Use of twisted 3-D Cauchy-condition surface to reconstruct the last closed magnetic surface in a non-axisymmetric fusion plasma

Masafumi ITAGAKI[1*], Gaku OKUBO[1], Masayuki AKAZAWA[1], Yutaka MATSUMOTO[1],

Kiyomasa WATANABE[2], Ryosuke SEKI[2], Yasuhiro SUZUKI[2]

[1]Graduate School of Engineering, Hokkaido University,

Kita 13, Nishi 8, Kita-ku, Sapporo 060-8628**,** Japan

[2]National Institute for Fusion Science, Toki 509-5292, Japan

This paper contains
27 pages of text,
7 tables and
24 figures.

*E-mail: itagaki@qe.eng.hokudai.ac.jp

Abstract

The three-dimensional (3-D) Cauchy condition surface (CCS) method code, ‘CCS3D’, is now under development to reconstruct the 3-D magnetic field profile outside a non-axisymmetric fusion plasma using only magnetic sensor signals. A new “twisted CCS” has been introduced, whose elliptic cross section rotates with the variation in plasma geometry in the toroidal direction of a helical type device. Independent of the toroidal angle, this CCS can be placed at a certain distance from the last closed magnetic surface (LCMS). With this new CCS, it is found through test calculations for the Large Helical Device that the numerical accuracy in the reconstructed field has been improved. Further, the magnetic field line tracing indicates the LCMS more precisely than with the use of the axisymmetric CCS. A new idea to determine the LCMS numerically has also been proposed.

Keywords: magnetic sensor, plasma boundary, last closed magnetic surface, Cauchy condition surface method, twisted Cauchy condition surface, vacuum field, boundary integral equation

PACS numbers: 28.52.-s, 28.52.Av., 52.55.-s, 52.55.Hc

1. Introduction

The identification of the MHD equilibrium configuration is important for the energy confinement and the stability of a nuclear fusion device from both operating control and analytical points of view. To identify the equilibrium configuration, (i) the pressure profile, (ii) the current profile and (iii) the plasma boundary shape or the last closed magnetic surface (LCMS) are three important parameters. They are often determined using the parameterization technique [1, 2] in such a way that an assumed correlation model satisfies the various measured data including the profiles of magnetic field, temperature and density, etc.

On the other hand, there is a different approach where one identifies the boundary shape independently of (i) the pressure and (ii) the current profile, deduced from signals of magnetic sensors located outside the plasma. This idea enables one to obtain accurate solutions of the boundary shape with a smaller amount of data than in the parameterization. One of such methods [3, 4] uses a small number of current “filaments” assumed at fixed positions within the plasma. The currents in these filaments are then computed in such a way that one obtains the best fit to the measured magnetic fluxes and fields. In contrast, a large number of filaments (beams) is assumed in the newer method proposed by J.Svensson and A.Werner [5]. With the use of a Bayesian approach, they inferred the distribution of possible flux surface topologies. Instead of such filaments, Feneberg et al. [6] assumed a “control surface” inside the plasma. The current density distribution on the surface is expressed as a sum of Fourier modes. Hofmann and Tonetti [7] proposed a method based on finite element basis functions to represent the plasma current distribution. Kurihara’s Cauchy condition surface (CCS) method [8, 9] has been established for real-time operating control and diagnosis of JT60U, a tokamak.

The works mentioned above focus mainly on tokamaks, i.e., axisymmetric plasmas, so that the analyses can be made in a 2-dimensional (2-D), r-z system. On the other hand, 3-D analyses are required for non-axisymmtric plasmas, e.g., in a helical type device such as the Large Helical Device (LHD) of the National Institute for Fusion Science (NIFS), Japan. In the LHD, it is important to consider the following characteristics of the plasma current:

(i) The plasma current itself is much weaker than the toroidal current in a tokamak device.

(ii) The dominant plasma current is the so-called Pfirsch-Schlüter current, the average of which over a magnetic surface vanishes. However, this current still has a 3-D profile.

Recently, the authors' research group developed the three-dimensional (3-D) Cauchy condition surface method [10] to reconstruct the 3-D magnetic field profile outside the plasma in the LHD. The work is the first extension of the CCS method to non-axisymmetric, 3-D fusion plasma. This 3-D analysis consumes a large number of unknowns, and then the problem becomes very ill-conditioned. The 10-fold rotational symmetry in the toroidal direction of the LHD was considered to reduce the number of unknowns. Also, the Tikhonov regularization technique was introduced to stabilize the solution. As a result, it was found that the magnetic field outside the plasma can be reconstructed with a fairly acceptable accuracy if a large number of magnetic sensors can be located outside the plasma. The magnetic field line tracing using this reconstructed field indicates fairly well the plasma boundary. However, the LCMS cannot necessarily be reconstructed clearly. To overcome this difficulty, one needs to improve the accuracy in the reconstructed field profile.

In the CCS method analysis, the choice of a suitable shape and size of the CCS is important to assure the accuracy of the reconstructed solution. In the previous work for the Large Helical Device (LHD) [10], the shape of the 3-D CCS was simply assumed to be a torus that has a circular cross section with radius 0.075m. Later, the authors found that a more accurate field reconstruction can be realized with a larger size of the CCS when the condition number is reduced to 10^5 (see section

4.1). At the same time the TSVD (Truncated Singular Value Decomposition) technique instead of Tikhonov's regularization technique was adopted since conveniently, the desired condition number can be specified directly in advance. Further, instead of the axisymmetric CCS, the authors introduced a new idea named "twisted CCS", where the elliptic cross section rotates with the variation in vacuum vessel geometry in the toroidal direction. Independent of the toroidal angle, the twisted CCS can keep a certain distance from its surface to the plasma boundary, so that a reduction in the numerical error can be expected.

This paper is arranged as follows. The outline of the 3-D CCS method is given in Section 2. Section 3 describes the twisted CCS and related computing techniques. Numerical demonstrations are shown in Section 4 to demonstrate the advantage of this new CCS model.

2. Outline of the 3-D CCS method

The CCS, where both the Dirichlet and the Neumann conditions are unknown, is hypothetically placed in a domain that can be supposed to be inside the plasma. In the analysis, no plasma current is assumed outside this CCS, where in reality plasma current does exist. Instead, the CCS plays the same role as the plasma current in causing the field outside the plasma.

A 3-D Cartesian coordinate system is adopted to realize a boundary-only integral formulation [10]. The first step of the analysis is to solve the following boundary integral equations (BIEs) and obtain the values of the vector potential and its derivative on the CCS in such a way that they will be consistent with the sensor signals [10].

(i) For magnetic field sensor locations i :

$$B_j - W_j^{(B)} = \sum_k \int_{\Gamma_{CCS}} \left\{ \left(L_k^j \phi_i^* \right) \frac{\partial A_k}{\partial n} - A_k \left(L_k^j \frac{\partial \phi_i^*}{\partial n} \right) \right\} d\Gamma. \quad (j = r, \varphi, z; \;\; k = x, y, z) \tag{1}$$

The operator L_k^j corresponds to a component in $\mathbf{B} = \nabla \times \mathbf{A}$ with $\mathbf{A}$ expressed in Cartesian coordinates, $W_j^{(B)}$ is the contribution of external coil currents, and ϕ_i^* the fundamental solution of the Laplace equation.

(ii) For flux loops:

For example, the BIE for a circle loop set in the toroidal direction is written as

$$\psi^{(Tor)} - W^{(Tor)} = \sum_k \int_{\Gamma_{CCS}} \left\{ \frac{\partial A_k}{\partial n} \left(\int_0^{2\pi} \eta_k \phi_i^* d\varphi \right) - A_k \left(\int_0^{2\pi} \eta_k \frac{\partial \phi_i^*}{\partial n} d\varphi \right) \right\} d\Gamma \qquad (k = x,\ y) \tag{2}$$

with $\eta_x = -R\sin\varphi$ and $\eta_y = R\cos\varphi$ for the radius R of the circle loop.

(iii) For points i on the CCS (Γ_{CCS}):

$$\frac{1}{2} A_{k,i} = \int_{\Gamma_{CCS}} \left(\phi_i^* \frac{\partial A_k}{\partial n} - A_k \frac{\partial \phi_i^*}{\partial n} \right) d\Gamma. \quad (k = x,\ y,\ z) \tag{3}$$

The above three types of BIEs are discretized, coupled and expressed in a matrix equation form. Considering the 10-fold rotational symmetry of the LHD in the toroidal direction, the number of unknowns is reduced by a factor of 10 with the aid of a linear transformation of the vector potential expressed in the Cartesian coordinate system [11]. One can now solve for all values of the Dirichlet condition (A_x, A_y, A_z) and the Neumann condition ($\partial A_x / \partial n$, $\partial A_y / \partial n$, $\partial A_z / \partial n$) on Γ_{CCS} in a least square sense. Once all the values of these conditions on the CCS are known, the magnetic fields for arbitrary points outside the CCS can be calculated using the formula

$$B_j = \sum_k \int_{\Gamma_{CCS}} \left\{ \left(L_k^j \phi_i^* \right) \frac{\partial A_k}{\partial n} - A_k \left(L_k^j \frac{\partial \phi_i^*}{\partial n} \right) \right\} d\Gamma + W_j^{(B)}. \qquad (j = r, \varphi,\ z;\ \ k = x, y, z) \tag{4}$$

3. Twisted Cauchy-condition surface method

3.1 Definitions of four regions

For the sake of the discussion from now on, the authors should give definitions of the LCMS and the following four regions. The LCMS in the present work means the outermost closed surface that is recognized through field line tracing with the Poincaré plot. Even outside the LCMS there exist

Poincaré plot points which are caused by the field lines that reach the divertor plate after many circulations around the torus. This field line region outside the LCMS is called the ‘stochastic region’ [12]. Outside this stochastic region is the ‘fully open field line region’. This is defined as a region where the traced field lines run away so promptly from the analytic domain that no Poincaré plot points are displayed. In other words, the connection lengths are extremely short in this region.

In addition, one here defines the following two regions as shown in figure 1 and table 1. The ‘dirty’ region is the domain sandwiched between the LCMS and the CCS. The ‘black’ region is the region inside the CCS, which is out of the analysis under consideration. That is, the use of equation (4) for drawing the field map is valid only outside the CCS.

In the CCS method analysis under the vacuum field assumption, the solutions are valid only for the fully open field line region (see the Appendix in Ref.[10]). In the stochastic region currents exist to some extent, but they are so weak that the accuracy of the field solution is fair. On the other hand, the reconstructed field in the dirty region, where a strong current density exists, has a large error which causes large scatters in the Poincaré plot.

Figure 1. Definitions of the four regions
Table 1. Features of the four regions

3.2 Drawback of the axisymmetric CCS

A larger cross-section of the CCS, i.e., a shorter distance between the CCS and the sensor positions is better for receiving the sensor signal information. However, the field solution inside the LCMS given by the CCS method includes error fields caused by neglecting the plasma current densities which extend beyond the LCMS and distort the field lines in the other regions (the stochastic and the fully open field line region). The effect of these error fields is smaller for a CCS

of smaller size. Because of this, the cross section of the axisymmetric CCS in the previous work [10] had to be set very small, i.e. a circle having 0.075m radius.

Figure 2. Images of the axisymmetric CCS and the twisted CCS

3.3 Introduction of the "twisted CCS"

To set the CCS closer to the sensor positions, one here introduces the "twisted CCS" as illustrated in figure 2, whose elliptic cross section rotates with the variation in vacuum vessel geometry in the toroidal direction. Independent of the toroidal angle, this CCS can be placed at a certain distance from the LCMS. A reduction in the numerical error can then be expected. The ellipse given by

$$\frac{(r-r_0)^2}{a^2}+\frac{(z-z_0)^2}{b^2}=1 \tag{5}$$

rotates 180° clockwise in the poloidal (θ) direction when it proceeds 36° counterclockwise in the toroidal (φ) direction following the 10-fold rotational symmetry of the LHD plasma. In this process the variation in the coordinates (r,z) on the CCS is described using the linear transformation

$$\begin{pmatrix} r-r_0 \\ z-z_0 \end{pmatrix}=\begin{pmatrix} \cos m\varphi & \sin m\varphi \\ -\sin m\varphi & \cos m\varphi \end{pmatrix}\begin{pmatrix} a\cos\theta \\ b\sin\theta \end{pmatrix}, \tag{6}$$

where m means the ratio $m=180°/36°=5$, φ and θ denote the toroidal angle and the poloidal angle, respectively ($0\le\theta\le180°$, $0\le\varphi\le36°$).

3.4 Truncated SVD technique

The three types of boundary integral equations shown in Section 2 are discretized, coupled and converted to a matrix equation that has the form

$$\mathbf{Dp}=\mathbf{g}, \tag{7}$$

where the solution vector $\mathbf{p}$ contains the vector potentials and their normal derivatives on the CCS. This equation is solved using the singular value decomposition (SVD) technique [13]. The matrix

$\mathbf{D}$ is decomposed as $\mathbf{D} = \mathbf{U}\mathbf{\Lambda}\mathbf{V}^{\mathrm{T}}$, where $\mathbf{U}$ and $\mathbf{V}^{\mathrm{T}}$ are orthogonal matrices and $\mathbf{\Lambda}$ is a diagonal matrix with positive singular values or zero components. In the previous work [10], the Tikhonov regularization technique [14] was employed to obtain a stabilized numerical solution. For the newly introduced twisted CCS, however, it was found that the truncated singular value decomposition (TSVD) technique [14] gave a better solution than the Tikhonov technique. In the TSVD technique, the regularized solution is given by

$$\mathbf{p} = \mathbf{V}\mathbf{\Lambda}_k^{-1}\mathbf{U}^{\mathrm{T}}\,\mathbf{g}\,. \tag{8}$$

Here $\mathbf{\Lambda}_k$ means that the singular values smaller than λ_k in $\mathbf{\Lambda}$ are omitted so that the condition number is not larger than a certain value.

3.5 Magnetic field line tracing

Once the 3-D magnetic field distribution has been obtained, the magnetic field line can be traced. This is performed using the MGTRC code [15]. Magnetic fields at any point are interpolated using a 3-D 4th order spline function. Equations of field lines are integrated with the use of an 8-stage 6th order Runge-Kutta formulation. The identification of the LCMS can be attempted with the process described in section 3.6.

3.6 Numerical determination of the LCMS

Even with the use of the twisted CCS, it is still difficult to discern the LCMS clearly by means of magnetic field line tracing. The authors propose a new idea to determine the LCMS numerically. Following this idea, the Poincaré plot is converted into contours of a ‘RBF-built function’ (see section 4.4.2) with the aid of the radial basis function (RBF) [16, 17]. One also introduces the ratio of the Poincaré plot scatter inside a contour of the RBF-built function to the scatter outside the contour. One will find the contour where this ratio jumps, which can be recognized as a good

estimate for the LCMS. The detailed process of the method will be described in sections 4.4.2 and 4.4.3.

3.7 Criteria for the analysis

The criteria for the present analysis of the field profile and its accuracy are as follows:

(i) A suitable size and shape of the CCS should be chosen for accurate and stable solutions.

(ii) The reconstructed field profile should have an acceptable accuracy in order to identify the plasma boundary and the LCMS through the field line tracing.

These two criteria have to be explored numerically.

4. Numerical demonstrations

One considers the plasma with the magnetic field strength, the magnetic axis location and the volume-averaged β being $B_{ax} = 3\mathrm{T}$, $R_{ax} = 3.6\mathrm{m}$ and $\langle\beta\rangle = 2.7\%$ respectively in the LHD. The reference MHD equilibrium for this condition had been analyzed beforehand [18] using the 3-D MHD equilibrium calculation code HINT2 [19]. That is, the magnetic sensor signals and the magnetic field caused by the external coil currents are known before the present analysis. The reconstructed results are compared with the reference solutions.

4.1 Calculation conditions

Figure 3 illustrates sensor locations in the *r*-*z* plane at the toroidal angle of 18 deg (the horizontally elongated cross-section). The black dots show the set of 100 magnetic flux loops in the toroidal direction, each of which is at a distance of 0.9m from the point $(r,\ z) = (3.7303\mathrm{m},\ 0.0\mathrm{m})$. The two circles depict the flux loops in the poloidal direction, which have radii of 1.0m and 1.2m

respectively with the center $(r, z) = (3.7303\text{m}, 0.0\text{m})$. A total of 26 flux loops of this type are set in 13 different *r*-*z* planes. The small circles illustrate the positions of 40 magnetic field sensors placed in this *r*-*z* plane. They are arranged a little way outside the LCMS. A total of 440 magnetic sensors are placed on 11 different *r*-*z* planes, but for convenience they are purposely placed within the range of toroidal angle, $0° \le \varphi \le 36°$. This arrangement of sensors is identical to the case where all of the sensors are distributed carefully for the whole range of $0° \le \varphi \le 360°$ in such a way that there will be no equivalent point under the 10-fold rotational symmetry. Each of the field sensors is assumed to detect all of the three components of magnetic field. All of the above sensor locations are exactly the same as those used in the previous work [10].

Figure 3. Sensor locations on the horizontally elongated cross-section

The calculation conditions and the corresponding results in the previous work are summarized as Case I in Table 2. An axisymmetric CCS having a 0.075m radius circular cross section was used, and the matrix equation (7) was solved using the Tikhonov regularization technique [14]. Later, the TSVD technique instead of Tikhonov's regularization was adopted since the desired condition number can be specified directly in advance.

The authors found that a more accurate field reconstruction can be realized with a larger size of CCS when the condition number is reduced to 10^5. That is, as stated in Case II in Table 2, better results were found for the axisymmetric CCS with $r = 0.150\text{m}$. Further, with the adoption of the twisted CCS where the values of a and b in equation (6) are 0.15m and 0.375m, respectively, the field solution accuracy is still more improved (Case III), so that the field line tracing also gives better results.

In the following, one simply uses the names 'axisymmetric CCS' case and 'twisted CCS' case for the calculation conditions in Case I and Case III, respectively. In both cases the center of each CCS

was set to be at $r = 3.7303\text{m}$ (major radius) and $z = 0.0\text{m}$. Considering a 10-fold rotational symmetry, only a 36-deg. portion of each CCS torus was modeled and this portion was divided into 48 discontinuous quadratic boundary elements, each of which has 9 nodal points [20]. Consequently, the number of unknowns is the product of the number of nodes ($N = 48 \times 9$), components of vector potential (=3) and boundary conditions at each nodal point (=2: the Dirichlet and the Neumann conditions). Thus it becomes $6N = 2592$, which is identical to the number of singular values.

Table 2 Calculation conditions and the corresponding results

4.2 Numerical errors in the reconstructed magnetic field

Figure 4 depicts the reference magnetic field profile on the horizontally elongated cross section. The three components on the left are the ones caused by the plasma current only, while the right three components are caused by both the plasma and the coil currents. Figure 5 shows the reconstructed magnetic field caused by plasma current only. The results using the axisymmetric CCS are on the left, while the ones using the twisted CCS are on the right. Figure 6 shows the relative errors for cases considering both plasma current and coil currents. Notice that extremely large values of this relative error are found at many places (some are over 10^5%). This is because the reference field values are under 10^{-5}T or exactly zero at some places (in red).

Figure 4. Reference magnetic field profile on the horizontally elongated cross section

Figure 5. Reconstructed magnetic field caused by plasma current only

Figure 6. Relative errors of magnetic field caused by both plasma current and coil currents

Table 3 summarizes the tendencies of the absolute errors in the magnetic field for the stochastic region on the horizontally elongated cross-section. Figures 7(a) and 7(b) also show the distributions of absolute error of B_φ obtained using the axisymmetric CCS and the twisted CCS respectively.

Table 3. Tendencies of the absolute errors in the stochastic region

Figure 7. Distribution of absolute error of B_φ.

The field errors near the LCMS are the most important for reconstruction of the LCMS. The absolute error distributions of B_φ within the region $1.0 < \rho < 1.1$ in the minor radius (ρ) space, i.e. very near the LCMS, are drawn in figure 8. Table 4 also summarizes the tendencies of the absolute errors of B_r, B_φ and B_z larger than 0.02T within the region $1.0 < \rho < 1.1$. It is found that the errors near the LCMS are drastically reduced when using the twisted CCS.

Figure 8. Absolute errors of B_φ near the LCMS

Table 4. Tendencies of the absolute field errors larger than 0.02T

4.3 Magnetic field line tracing

Based on the reconstructed field, magnetic field line tracings were carried out. Equation (4) is used for reconstructing the required 3-D field distribution. The use of equation (4) is valid only outside the CCS. The large errors inside the CCS are caused by the wrong use of equation (4). At a point outside the CCS but very close to the CCS there is a possibility that the fundamental solution becomes near singular. However, the main reason for the dirty solution outside the CCS is the hypothetical “vacuum field” assumption for the plasma region. This becomes clear by comparing figure 7(b) with figure 22(a) and 22(b), which will be given in section 4.5.5. That is, the portion of

area where the error is larger than 0.050T (highlighted in red) increases with the $\langle\beta\rangle$ value. To avoid a numerical instability caused by the dirty solution, the three components of the field caused by the plasma current had all been set to be zero at the points where the root mean square $\sqrt{B_r^2 + B_\varphi^2 + B_z^2}$ exceeds 0.1(T). That is, the authors assumed the vacuum field at these points (notice that this treatment had not yet been applied in figures 7(a) and 7(b)).

The starting points (r, z, φ) of the traces were set as

$$r = 4.30 + 0.01k \quad \text{in [m] with} \quad k = 0, 1, \cdots, 40,$$

$z = 0.0\text{m}$ and $\varphi = 18°$ (the horizontally elongated cross section). Each trace was terminated when the number of toroidal transits reached 100 or when the field line ran out of the analytic domain under consideration. Figures 9(a), 9(b) and 9(c) are the Poincaré plots of the field line on the r-z plane at $\varphi = 18°$. Figure 9(a) is given from the reference field, while figure 9(b) and figure 9(c) are the reconstructed results when using the axisymmetric CCS and the twisted CCS, respectively.

Either with the axisymmetric CCS or with the twisted CCS, the reconstructed outer surface of the stochastic region shows a good agreement with the reference one. This fact can be supported by the mathematical background that theoretically outside the plasma region the CCS method solution under the vacuum field assumption agrees with the solution which takes into account the existence of plasma current (see the appendix in Ref.(9)). It should also be pointed out that in both figure 9(b) and figure 9(c) even marks of the divertor legs are reconstructed.

Figure 9. Poincaré plots of the field line (1): Stochastic region

Figures 10(a) and 10(b) highlight the Poincaré plots on the r-z plane at $\varphi = 18°$ for traces originating at the same starting point $(r, z, \varphi) = (4.47\text{m}, 0.0\text{m}, 18°)$, which formed the LCMS when following the reference field. In each figure, the dashed closed line shows the LCMS for the

vacuum field, i.e., $\langle\beta\rangle = 0\%$. This is shifted outward when $\langle\beta\rangle$ takes the nonzero value $\langle\beta\rangle = 2.7\%$. The reference LCMS in this case is the solid closed line.

In figure 10(a), the red round symbols show the results of the trace originating at the same starting point as the reference LCMS for $\langle\beta\rangle = 2.7\%$, but based on the reconstructed field obtained using the axisymmetric CCS. They do not form a sharp closed surface, however, the round symbols are distributed almost along the reference LCMS for $\langle\beta\rangle = 2.7\%$.

The results based on the twisted CCS are shown in figure 10(b). The scatter of the plot points is narrower than in the case of the axisymmetric CCS, i.e., the accuracy in the reconstruction has been significantly improved.

Figure 10. Poincaré plots of the field line (2): LCMS

4.4 Numerical determination of the LCMS

Hereafter, the discussion is limited to the case using the twisted CCS. As shown in the previous section, the Poincaré plot based on the reconstructed field did not form the LCMS clearly. In this section one discusses an idea to estimate where the LCMS is.

4.4.1 Connection length

Figure 11 illustrates the variation in the connection length as a function of the r-coordinate of the starting point, r_{start}. It can be stated that the field line forming the LCMS has a starting point with r_{start} less than or equal to 4.53m, where the connection length can still be considered infinite.

Figure 11. Variation in the connection length

4.4.2 Contour surfaces of RBF-built function

The field line traces in the present work originated at the starting points that were indicated in section 4.3. Ideally, the r-coordinate of the starting point can be recognized as a label that corresponds to each magnetic surface if it is a true surface. That is, $r_{start}^{(k)} = \psi(r_{start}^{(k)},\, z_{start}^{(k)})$ with

$$z_{start}^{(k)} = 0 \quad \text{and} \quad r_{start}^{(k)} = 4.30 + 0.01k \quad \text{in [m] with} \quad k = 0, 1, \cdots, K\,.$$

With this idea, the set of discrete Poincaré plot points can be converted to a contour map as a function of $r_{start}^{(k)}$. One here introduces the radial basis function (RBF) expansion [16, 17]

$$\psi(r,z) = \sum_{i=1}^{N} w_i\, f_i(r,z;r_i,z_i) \tag{9}$$

with the Gaussian type RBF

$$f_i\left(r,z;\, r_i,z_i\right) = \exp\left\{-\left(\left(r-r_i\right)^2 + \left(z-z_i\right)^2\right)\Big/\sigma^2\right\}, \tag{10}$$

where (r_i, z_i) means the center of each RBF, σ the scaling factor and N the number of RBFs. The centers of 100 RBFs, (r_i, z_i), were distributed equidistantly in the rectangle domain ($2.2\text{m} < r < 5.2\text{m},\ -1.5\text{m} < z < 1.5\text{m}$), i.e., with a grid spacing of $\Delta r_i = \Delta z_i = 0.3[\text{m}]$. The scaling factor was chosen as $\sigma = 1.0\text{m}$.

The unknown weights w_i are determined by solving the matrix equation

$$\begin{bmatrix} f_{1,1} & f_{1,2} & \cdots & f_{1,N-1} & f_{1,N} \\ f_{2,1} & f_{2,2} & \cdots & f_{2,N-1} & f_{2,N} \\ f_{3,1} & f_{3,2} & \cdots & f_{3,N-1} & f_{3,N} \\ \vdots & \vdots & \ddots & \vdots & \vdots \\ f_{M-1,1} & f_{M-1,2} & \cdots & f_{M-1,N-1} & f_{M-1,N} \\ f_{M,1} & f_{M,2} & \cdots & f_{M,N-1} & f_{M,N} \end{bmatrix} \begin{Bmatrix} w_1 \\ w_2 \\ \vdots \\ w_{N-1} \\ w_N \end{Bmatrix} = \begin{Bmatrix} \psi_1 \\ \psi_2 \\ \psi_3 \\ \vdots \\ \psi_{M-1} \\ \psi_M \end{Bmatrix} \tag{11}$$

in a least square manner. In more detail, the SVD technique is used with the Tikhonov regularization technique (the value of Tikhonov regularization parameter was $\gamma = 10^{-15}$ [14]). In equation (11), $f_{m,i}$ denotes $f_i(r_m, z_m; r_i, z_i)$ for the Poincaré plot point (r_m, z_m) $(m = 1, 2, \cdots, M)$, where M denotes the total number of plot points ($M > K$). The quantity ψ_m corresponds to the point (r_m, z_m) but takes the value of its original starting point, i.e., one of $r_{start}^{(k)}$ $(k = 1, 2, \cdots, K)$.

With the use of the RBFs, the reconstructed Poincaré plot shown in figure 9(c) can be converted into contours of RBF-built function that is shown in figure 12. For convenience, one here names each contour the 'quasi' magnetic surface. Contours are found even outside the LCMS in figure 12, however, they are not true magnetic surfaces.

In addition, the contours found deep inside the LCMS should be ignored. They are meaningless and just the result of interpolation of the RBF expansion, for which the Poincaré plot points originated at $r_{start} < 4.30$ were not adopted as the sampling points, i.e., not included in the set of (r_m, z_m) $(m = 1, 2, \cdots, M)$.

Figure 12. Contours of RBF-built function

The red symbols in figures 13(a) and 13(b) show the Poincaré plot originating from start point at $r_{start} = 4.55\text{m}$ and $r_{start} = 4.52\text{m}$, respectively. The black line on each figure depicts the quasi magnetic surface for the corresponding starting point. However, they are not true magnetic surfaces but are outside the true LCMS, which is stated in Section 4.3 to correspond to $r_{start} = 4.47\text{m}$. It should be noted that these two Poincaré plots are discontinuous along each quasi magnetic surface and one finds many gaps. This suggests that even with the present 3-D CCS reconstruction method it is possible to recognize the existence of magnetic islands (see section 4.5.4).

Figure 13. Poincaré plot with the quasi magnetic surface outside the LCMS

Figure 14 shows three patterns of the Poincaré plot with the quasi magnetic surface near the LCMS, specifically $r_{start} = 4.48\text{m}, 4.47\text{m}$ and 4.46m. For $r_{start} = 4.48\text{m}$ and $r_{start} = 4.47\text{m}$, the plots are slightly scattered along the quasi magnetic surface. However, in figure 14(c), the plots are scattered widely inside the surface that corresponds to $r_{start} = 4.46\text{m}$. This phenomenon can be explained as follows. The plasma current density is weak outside this surface (the stochastic region), while a

strong current density exists inside the LCMS so that the reconstructed magnetic field profile is very dirty due to the hypothetical vacuum field assumption in the CCS method analysis (see the definition of the dirty region in section 3.1). Because of this, the magnetic field line trace takes irregular courses inside the dirty region. There is a possibility, however, that this difference between the scatters inside and outside the surface can be used as an indicator to judge where the LCMS might be.

Figure 14. Poincaré plot with the quasi magnetic surface near the LCMS

4.4.3 Method of 'inside/outside' ratio

One here introduces the 'scatter' given by

$$s^2 = \frac{1}{m}\sum_{j=1}^{m} d_j{}^2, . \tag{12}$$

Where d_j denotes the distance between a reconstructed contour (quasi magnetic surface) and the *j*-th point in the *m* Poincaré plot points corresponding to the quasi magnetic surface. Next, one defines the 'inside/outside' ratio as

$$R = s^2_{inside} \big/ s^2_{outside} \tag{13}$$

with s^2_{inside} and $s^2_{outside}$ being the scatters calculated using Eq.(12) respectively for the points inside and outside of the contour under consideration.

Figure 15 shows the variation in the 'inside/outside' ratio as a function of r_{start}. The ratio jumps where r_{start} is reduced to a value smaller than 4.47m. Because of this, one can conjecture that the most probable location of the LCMS corresponds to $r_{start} = 4.47m$.

Figure 15. Variation in the 'inside/outside' ratio

Among the contours in figure 12, which were drawn by the RBF expansion scheme, the contour corresponding to $r_{start} = 4.47m$ was extracted. This estimated LCMS agrees well with the reference LCMS as shown in figure 16.

Figure 16. Reconstructed LCMS

4.5 Some other test calculations

This section describes the results of some additional calculations. The calculation conditions other than the conditions specified in each test item are the same as those in the analysis for the standard twisted CCS case that were given in Section 4.1. Also, the profiles of fields and errors will be depicted only on the horizontally elongated cross section.

4.5.1 Effect of flux loop signals

The detailed variation in 3-D vector potential along the flux loop is eliminated by the loop integral. The flux loop signals are, so to speak, auxiliary information or constraints. On the other hand, in the authors' experience the use of only field sensors in the 3-D space could give fair (not meaningless) solutions for the field. However, the accuracy of the reconstructed field is apparently lowered as shown in figure 17, compared with the standard case where both the flux loops and the field sensors are considered (see figures 5(b) and 7 in Section 4.2). Table 5 also sumarizes the difference in error tendency between the cases where the flux loops are considered and not considered.

Figure 17. Reconstructed B_{φ} and its absolute error when the flux loops are not considered

Table 5 Effect of flux loop signals

4.5.2 Influence of the sensor signal noise

The effect of measurement errors on the reconstruction was also studied. Noises were numerically generated using normal (Gaussian) random numbers and added to all magnetic field and flux loop signals. That is, the relationship between a noise-added signal $\tilde{b}_j$ and its original signal b_j is given by $\tilde{b}_j = b_j(1+\sigma \cdot G)$, where G denotes a unit Gaussian random number, while σ the standard deviation of the Gaussian noise. Figure 18(a) shows the change in the maximum errors of B_r, B_φ and B_z as a function of σ, while figure 18(b) indicates the variation in the portion of the area where the error is larger than 0.02T. Both error tendencies were investigated for the region $1.0 < \rho < 1.1$ in the minor radius (ρ) space, i.e. very near the LCMS. It is understood from these results that the reconstructed field profile is not very sensitive to the noise in the sensor signals since the CCS method is made in a least square sense. If we assume that the total signal error caused by the signal fluctuation and the sensor dislocation is no more than a few percent, it would not adversely influence the reconstructed field.

Figure 18. Influence of the sensor signal noise

4.5.3 Reduction in the number of sensors and boundary elements

It is impractical to assume such a large number of sensors (440 field sensors and 126 flux loops) as described in section 4.1. However, considering the stellarator-symmetry

$$B_r(r,\ z,\ -\varphi) = -B_r(r,\ -z,\ \varphi), \tag{14a}$$

$$B_z(r,\ z,\ -\varphi) = B_z(r,\ -z,\ \varphi) \tag{14b}$$

and

$$B_\varphi(r,\ z,\ -\varphi) = B_\varphi(r,\ -z,\ \varphi) \tag{14c}$$

and the up-down symmetry as well in the LHD, the 440 field sensors located within a 36 degree range are automatically reduced by half or less without remodeling the computer code. Also, the condition $B_r = 0$ can be considered to be at $z = 0$ on the 0 degree and 18 degree planes.

Another possibility to reduce the number of sensors is to reduce the number of unknowns, i.e., the number of boundary elements. The authors carried out a test calculation with only 20 boundary elements. In this case the number of sensors could be reduced by half. Although the B_φ profile shown in figure 19 roughly keeps the original tendency (see figure 5(b) and figure 7), the solution accuracy shown in Table 6 was apparently lower than before.

It is important to have a number of sensor signals available which is large enough for the numerical problem. If so many sensors cannot be actually set up, it is worth considering interpolations of sensor signals, i.e., creating 'virtual' sensors from the signals of nearby real sensors. The authors would like to consider this as one of their further works.

Figure 19. Reconstructed B_φ and its absolute error when the number of sensors and the number of boundary elements are reduced

Table 6. Reduction in the number of sensors and boundary elements

4.5.4 Magnetic islands

Figure 13 suggested that one can find magnetic islands even with the present CCS reconstruction method. To define the islands more clearly, the field line tracings based on the reconstructed field were carried out for a large number of starting points. When the tracing started at the point $(r_{start},\ z_{start}) = (4.40\text{m},\ 0.177\text{m})$ on the horizontally elongated cross section, islands were found as indicated by the black dots in figure 20(a). The red marks in figure 20(a) are the plots in figure 13(a) and 13(b), i.e., the plots for the starting points $(r_{start},\ z_{start}) = (4.55\text{m},\ 0.0\text{m})$ and $(r_{start},\ z_{start}) = (4.52\text{m},\ 0.0\text{m})$, respectively. It can be seen that they go past the shoulders of the

islands. These reconstructed islands are compared with the islands obtained from the reference field. The green dots in figure 20(b) are the reference islands. In this reference case, the starting point was $(r_{start}, z_{start}) = (4.40\text{m}, 0.171\text{m})$. Figures 20(c) and 20(d) are enlarged pictures of islands (A) and (B) respectively in figure 20(b). The positions of the reconstructed islands are not exactly the same as the reference ones, but the tendency is almost the same.

Figure 20. Magnetic islands

4.5.5 Method of 'inside/outside' ratio for low β plasmas

The method of 'inside/outside' ratio shown in section 4.4.3 is, so to speak, a way of turning the numerical dirtiness of the region inside the LCMS to our own advantage. The scheme is based on the assumptions:

(i) A certain amount of Pfirsch-Schlüter current exists inside the LCMS and causes the numerical dirtiness and hence the large scatter in the Poincaré plot inside the LCMS due to the vacuum field assumption in the CCS method.

(ii) There is much difference in the level of numerical dirtiness between the regions inside and outside the LCMS, i.e., the currents outside the LCMS region should be much weaker.

Considering the assumptions, it should be tested whether the method ends in failure for a low β plasma configuration.

The test calculation for the plasma with $\langle\beta\rangle = 2.7\%$ described in Section 4.4 was repeated for plasmas with $\langle\beta\rangle = 1.0\%$ and $\langle\beta\rangle = 2.0\%$ in the LHD. Figure 21 shows the profiles of the reference and the reconstructed magnetic field caused by the plasma current only with $\langle\beta\rangle = 1.0\%$. Absolute errors in the reconstructed B_φ are shown in figure 22 for both cases with $\langle\beta\rangle = 1.0\%$

and $\langle\beta\rangle = 2.0\%$. Table 7 also summarizes the absolute tendency. Due to the weak plasma current, the errors in the case of $\langle\beta\rangle = 1.0\%$ are comparatively small. The same CCS location, which is at almost the center of the LCMS for $\langle\beta\rangle = 2.7\%$, is again used for $\langle\beta\rangle = 1.0\%$ and 2.0%, so that the CCS is relatively shifted outward from the center of the LCMS (see figure 22). Because of this, the errors for $\langle\beta\rangle = 2.0\%$ are not always lower than those for $\langle\beta\rangle = 2.7\%$.

Figure 21. Profiles of the reference and the reconstructed magnetic field caused by the plasma current only with $\langle\beta\rangle = 1\%$
Figure 22. Absolute errors in the reconstructed B_φ for low β plasmas
Table 7. Effect of the difference in β value

The procedure described in section 4.4 was repeated for the cases: $\langle\beta\rangle = 1.0\%$ and $\langle\beta\rangle = 2.0\%$. After obtaining the Poincaré plot points, the variation in the 'inside/outside' ratio was calculated as shown in figure 23. The ratio jumps at $r_{start} = 4.38\text{m}$ for the $\langle\beta\rangle = 1.0\%$ case, while the ratio jumps at $r_{start} = 4.41\text{m}$ for the $\langle\beta\rangle = 2.0\%$ case. The contours of RBF-built function corresponding to these starting points were extracted as shown in figure 24(a) and 24(b). On the other hand, through careful investigation the reference LCMS was recognized to be corresponding to $r_{start} = 4.40\text{m}$ for both $\langle\beta\rangle$ value cases. However the inboard side of the LCMS is shifted outward (from $r = 2.92\text{m}$ to 3.00m) with the increase in the $\langle\beta\rangle$ value. A similar tendency in the LHD plasma was reported by Watanabe et al. [21]. The value of r_{start} indicated in each reconstruction for such a low β plasma does not agree exactly with the reference value, however, the authors believe that the accuracy of each extracted LCMS shown in figure 24 is acceptable at least for operating control purposes.

However, to demonstrate that the scheme will in general give reliable results, it is important to carry out numerical tests for a large number of field configurations in the LHD or for different devices. For example, it is worth investigating cases where the magnetic axis is located at positions different from $R_{ax} = 3.6\mathrm{m}$ in the LHD.

Figure 23. Variation in the 'inside/outside' ratio for low β plasmas
Figure 24. Reconstructed LCMS for low β plasmas

4.6 Some comments

4.6.1 Sensor locations

In actual fusion devices there are some places where it is difficult to set sensors. In the LHD, with the existence of big ports, one should pay attention to the setup of flux loops and magnetic probes near the X-points. However, we can find a way out of this difficulty. First, the shape of a flux loop need not be a complete circle. Next, the density of magnetic probes to be set near the X-point is somewhat limited but one can interpolate the field signals of nearby magnetic probes and create information at the missing locations. Of course it is unknown whether these countermeasures will not reduce the information. This problem deserves more investigation.

Incidentally, in general, one can consider the 10-fold rotational symmetry, the stellarator-symmetry and the up-down symmetry for setting sensors at suitable positions.

4.6.2 Applicability to other devices

The CCS method is based on the boundary element method that can be applied to any irregular geometry. Because of this, we can work with any model of CCS geometry. Also, from a mathematical point of view, the reconstructed solution is not very sensitive to the position of the CCS. The center of the CCS need not agree with the magnetic axis or the geometrical center. In fact,

the CCS shown in figures 21 and 22 is not located at the center but shifted outward. The method is in principle also applicable to a system with a non-planar axis.

5. Conclusion and further remarks

With the use of the twisted CCS rather than the axisymmetric CCS, the numerical accuracy in the reconstructed field has been improved.

The magnetic field line tracing indicates that either with the axisymmetric CCS or with the twisted CCS, the reconstructed outer surface of the stochastic region shows a good agreement with the reference one. With the twisted CCS, the scatter of the Poincaré plot points along the LCMS is narrower than in the case with the axisymmetric CCS, i.e., the accuracy has been significantly improved.

A numerical technique to determine the LCMS has also been proposed. The Poincaré plot is converted to contours of a RBF-built function using the RBF expansion. Introducing the 'inside/outside' ratio related to the scatter in the Poincaré plot, the contour where the ratio jumps is taken as a best estimate for the location of the LCMS, which agrees well with the reference LCMS.

It should be stressed that all the above results have been reconstructed using only magnetic sensor signals. On this occasion, the authors would like to give the simple name 'CCS3D' to the FORTRAN code describing the present 3-D CCS method. The LHD was dealt with as a numerical example in this paper, but no special assumption peculiar to the LHD is included in the CCS3D code. Generally speaking, the CCS3D code is applicable to any non-axisymmetric fusion plasma.

The authors are now considering the following as further tasks:

(i) Development of a numerical technique to create 'virtual' sensors by interpolating the signals of nearby real sensors. This is to compensate for the small number of genuine sensors in an actual device

(ii) More numerical tests for a large number of field configurations in the LHD or for different devices in order to demonstrate that the present method will in general give reliable results. It is worth investigating cases where the magnetic axis is located at positions different from $R_{ax} = 3.6\text{m}$ in the LHD.

(iii) Guidelines for the best regularization in the SVD technique are still worth investigating.

Acknowledgments

This research was performed with the support and under the auspices of the NIFS Collaboration Research Program (NIFS08KLPP015). This work was also supported by the Ministry of Education, Culture, Sports, Science and Technology, Grant-in-Aid for Scientific Research (C), 20560762, 2010.

References

[1] Braams, B.J., Jilge, W. and Lackner, K. 1986 *Nucl. Fusion*, **26**, 699

[2] Callaghan, H.P., McCarthy, P.J. and Geiger, J. 1999 *Nucl. Fusion*, **39**, 509

[3] Lao, L.L., St. John, H., Stambaugh, R.D. and Pfeiffer, W. 1985 *Nucl. Fusion*, **25**, 1421

[4] Swain, D.W and Neilson, G.H. 1982 *Nucl. Fusion*, **22**, 1015

[5] Svensson, J., Werner, A. and JET-EFDA Contributors. 2008 *Plasma Phys. Control. Fusion* **50** 085002

[6] Feneberg, W., Lackner, K. and Martin, P. 1984 *Comp. Phys. Commun*., **31**, 143

[7] Hofmann, F. and Tonetti, G. 1988 *Nucl. Fusion*, **28**, 519

[8] Kurihara, K. 2000 *Fusion Eng. Des.* **51-52** 1049

[9] Itagaki, M., Yamaguchi, S. and Fukunaga, T. 2005 *Nucl. Fusion* **45** 153

[10] Itagaki, M., Maeda, T., Ishimaru, T., Okubo, G., Watanabe, K., Seki, R. and Suzuki, Y. 2011 *Plasma Phys. Control. Fusion* **53** 105007

[11] Itagaki, M., Ishimaru, T. and Watanabe, K. 2010 *Proc. the 32nd International Conf. on Boundary Elements and Other Mesh Reduction Methods*, (Southampton, U.K., 2010), (WIT Press, Southampton, U.K.) p.133

[12] Matsumoto. Y., Oikawa, S., Watanabe, T. 2002 *J. Phys. Soc. Jpn* **71** 1684

[13] Press, W.H., Flannery, B.P., Teukolsky, S.A. and Vetterling, W.T. 1986 *Numerical Recipes - The Art of Scientific Computing* (Cambridge: Cambridge University Press)

[14] Hansen, P.C. 1998 *Rank-Deficient and Discrete Ill-Posed Problems – Numerical Aspects of Linear Inversion* (Philadelphia: SIAM)

[15] LHD Experimental Board 2009 *Section 6 LHD Experiment Technical Guide 2009* (Toki, Japan: National Institute for Fusion Science)

[16] Buhmann, M. D. 2003 *Radial Basis Function* (Cambridge: Cambridge University Press).

[17] Itagaki, M., Nakata, K. Tanaka, H. and Wakasa, A. 2009 *Engineering Analysis with Boundary Elements* **33**, 1258

[18] Seki, R., Matsumoto, Y., Suzuki, Y., Watanabe, K. and Itagaki, M. 2008 *Plasma Fusion Res.* **3** 016

[19] Suzuki, Y., Nakajima, N., Watanabe, K., Nakamura, Y. and Hayashi, T. 2006 *Nucl. Fusion* **46** L19

[20] Itagaki, M., Sahashi N. 1996 *J. Nucl.Sci. Technol.* **33** 7

[21] Watanabe, K.Y., Suzuki, Y., Sakakibara, S. et al. 2010 *Fusion Sci. Technol.* **58** 160

Table 1. Features of the four regions

Region	Current density	Accuracy of the reconstructed field
Fully open field line	No	Acceptable
Stochastic	Weak	Fair
“Dirty”	Strong	Large error
“Black”	Strong	Out of the analysis

Table 2 Calculation conditions and the corresponding results

		I	II	III
Regularization technique		Tikhonov’s $\gamma = 10^{-14}$	TSVD Condition No. □ 10^5	TSVD Condition No. □ 10^5
CCS model		Axisymmetric CCS (r=0.075m)	Axisymmetric CCS (r=0.150m)	Twisted CCS (a=0.150m, b/a=2.5)
Maximum error	B_r	0.028	0.039	0.030
	B_φ	0.055	0.015	0.024
	B_z	0.022	0.040	0.022
Portion of area where $\varepsilon > 0.02$T	B_r	11.5%	12.5%	4.2%
	B_φ	10.4%	0.0%	5.2%
	B_z	5.2%	10.4%	4.2%
Original Cond. No.		3.7486E+16	3.0982E+16	3.4098E+13
Modified Cond. No.		7.0097E+06	9.9041E+04	9.8656E+04

The values related to the errors are evaluated within the region very near the LCMS ($1.0<\rho<1.1$ in the minor radius (ρ) space).

Table 3. Tendencies of the absolute errors in the stochastic region

	Axisymmetric CCS			Twisted CCS		
No. of points for the specified region	307			307		
	B_r	B_φ	B_z	B_r	B_φ	B_z
$\varepsilon < 0.01$(T)	75.9%	62.5%	58.3%	83.1%	65.1%	68.1%
$\varepsilon < 0.005$(T)	45.9%	24.4%	28.3%	52.1%	27.0%	29.3%
$\varepsilon < 0.001$(T)	8.8%	5.5%	8.5%	14.0%	3.6%	5.2%
Max. Error (T)	0.028	0.055	0.022	0.030	0.024	0.022
Ave. Error (T)	0.007	0.009	0.009	0.006	0.008	0.009

Table 4. Tendencies of the absolute field errors larger than 0.02T

Region	$1.0 < \rho < 1.1$ (Outside the LCMS)	
No. of points	96	
Points where $\varepsilon > 0.02$(T)	Axisymmetric CCS	Twisted CCS
B_r	11 (11.5%)	4 (4.2%)
B_φ	10 (10.4%)	5 (5.2%)
B_z	5 (5.2%)	4 (4.2%)

Table 5 Effect of flux loop signals

		Flux loop Considered	Flux loop Not considered
Maximum error (T)	B_r	0.030	0.048
	B_φ	0.024	0.051
	B_z	0.022	0.048
Portion of area where $\varepsilon > 0.02$T	B_r	4.2%	25.0%
	B_φ	5.2%	15.6%
	B_z	4.2%	27.1%

The errors are evaluated within the region very near the LCMS ($1.0<\rho<1.1$ in the minor radius (ρ) space) on the horizontally elongated cross section.

Table 6 Reduction in the number of sensors and boundary elements

No. of boundary elements (No. in the toroidal direction) (No.in the poloidal direction)		48 (8) (6)	20 (5) (4)
No. of field sensors		440	220
No. of flux loops: in the toroidal direction in the poloidal direction		 100 26	 50 13
Maximum error (T)	B_r B_φ B_z	0.030 0.024 0.022	0.071 0.024 0.058
Portion of area where $\varepsilon > 0.02$T	B_r B_φ B_z	4.2% 5.2% 4.2%	38.5% 5.2% 41.7%
Original Cond. No.		3.4098E+13	1.7731E+09
Modified Cond. No.		9.8656E+04	9.9313E+04

The errors are evaluated within the region very near the LCMS (1.0<ρ<1.1 in the minor radius (ρ) space) on the horizontally elongated cross section.

Table 7 Effect of the difference in β value

	$\langle\beta\rangle$	1.0%	2.0%	2.7%
Maximum error (T)	B_r B_φ B_z	0.012 0.006 0.012	0.039 0.022 0.022	0.030 0.024 0.022
Portion of area where $\varepsilon > 0.02$T	B_r B_φ B_z	0.0% 0.0% 0.0%	10.4% 2.1% 2.1%	4.2% 5.2% 4.2%

The errors are evaluated within the region very near the LCMS (1.0<ρ<1.1 in the minor radius (ρ) space) on the horizontally elongated cross section.

List of Figures

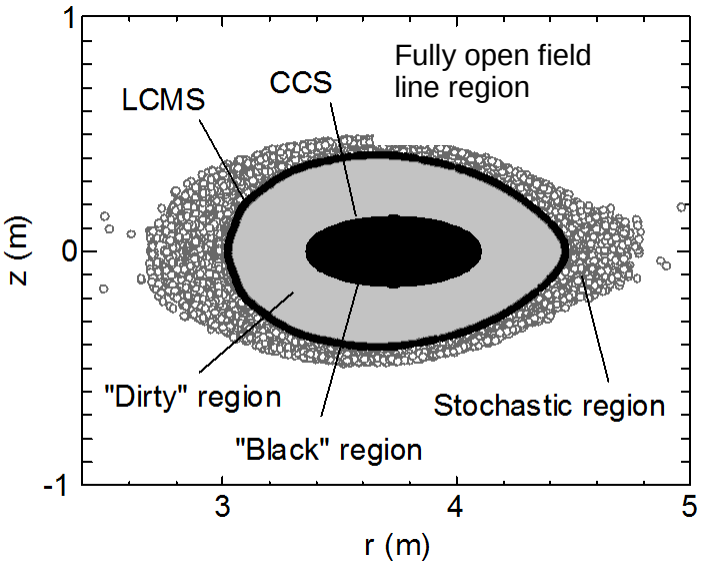

Figure 1. Definitions of the four regions

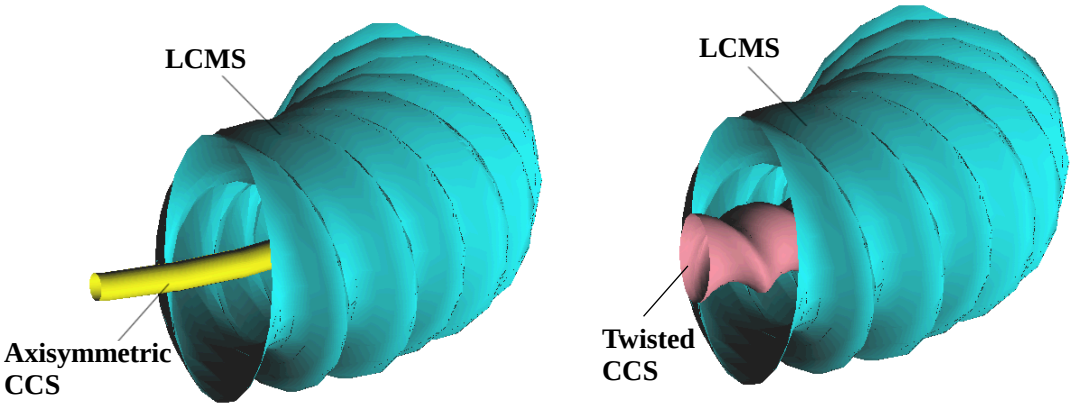

(a) Axisymmetric CCS (b) Twisted CCS

Figure 2. Images of the axisymmetric CCS and the twisted CCS

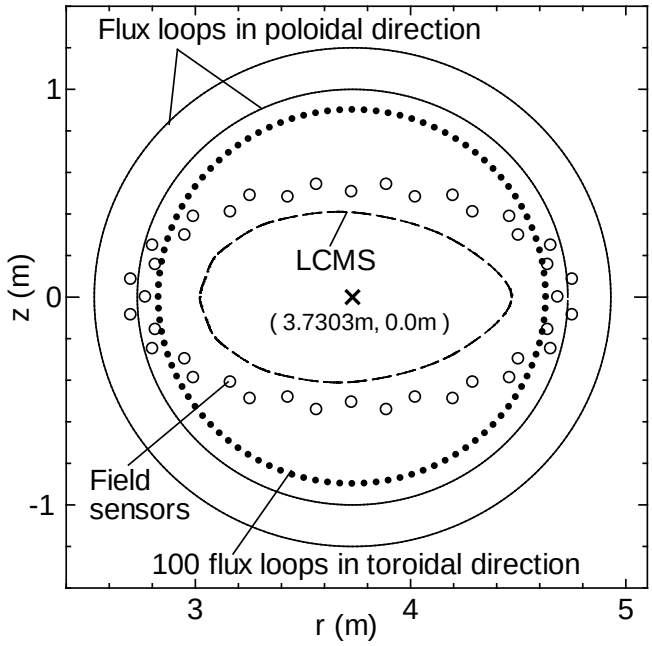

Figure 3. Sensor locations on the horizontally elongated cross-section

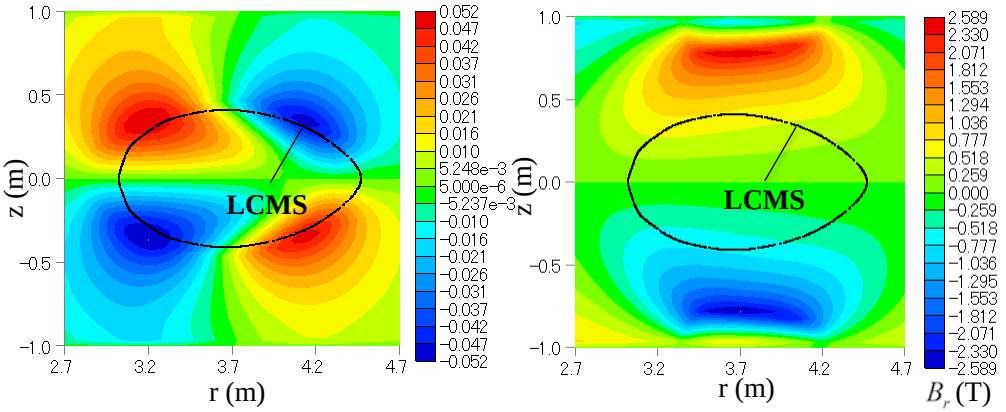

(a) B_r (Left: caused by plasma current only. Right: coil current effect is added.)

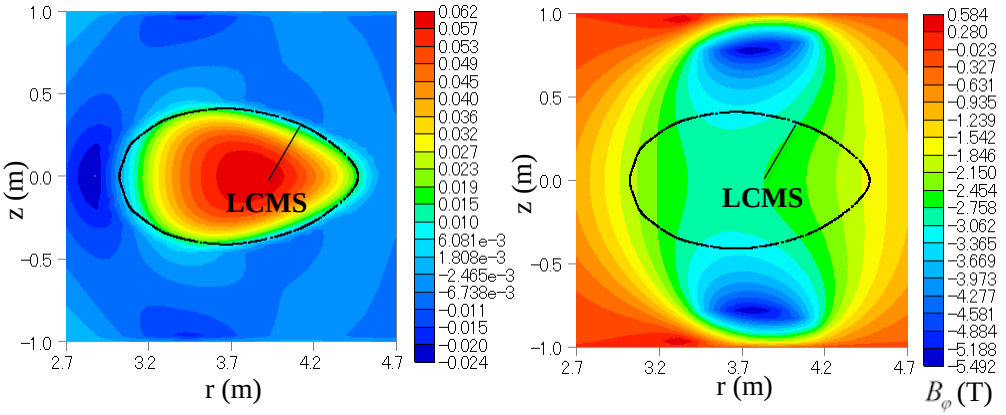

(b) B_φ (Left: caused by plasma current only. Right: coil current effect is added.)

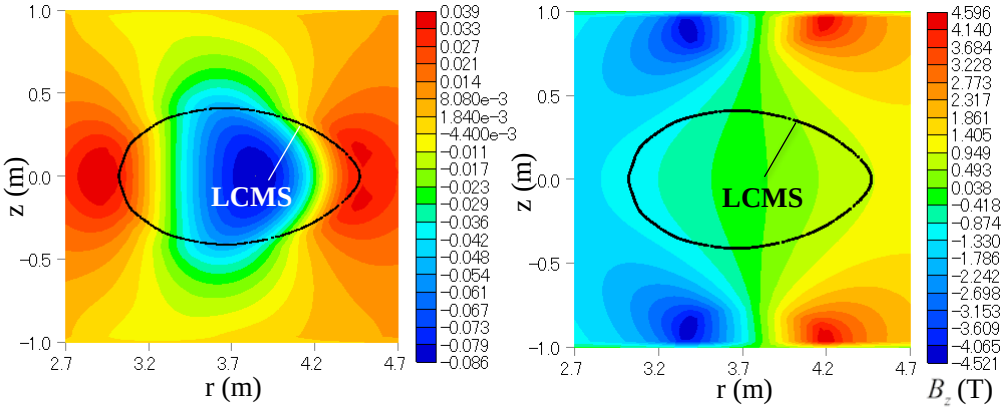

(c) B_z (Left: caused by plasma current only. Right: coil current effect is added.)

Figure 4. Reference magnetic field profile on the horizontally elongated cross section

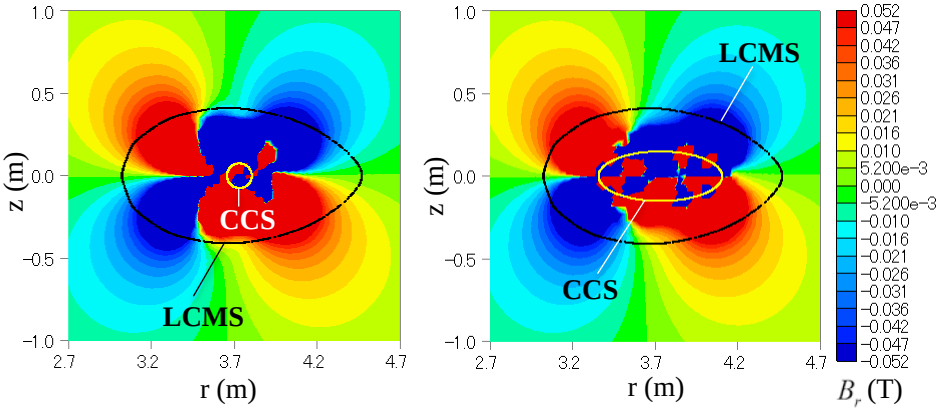

(a) B_r (Left: using the axisymmetric CCS. Right: using the twisted CCS.)

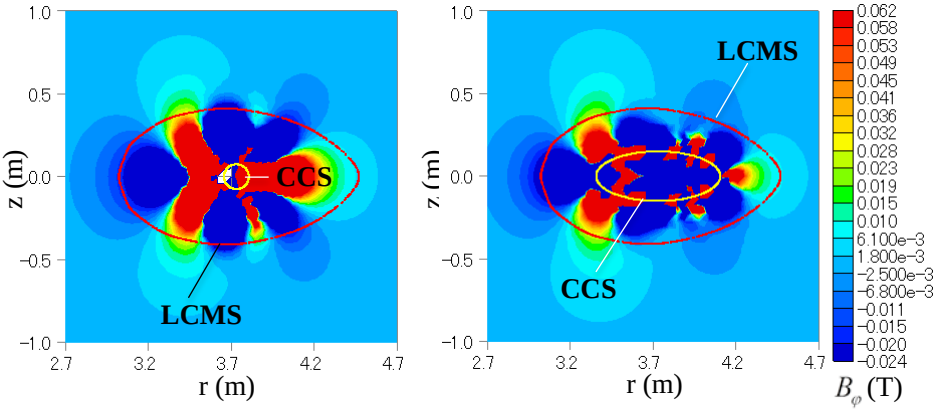

(b) B_φ (Left: using the axisymmetric CCS. Right: using the twisted CCS.)

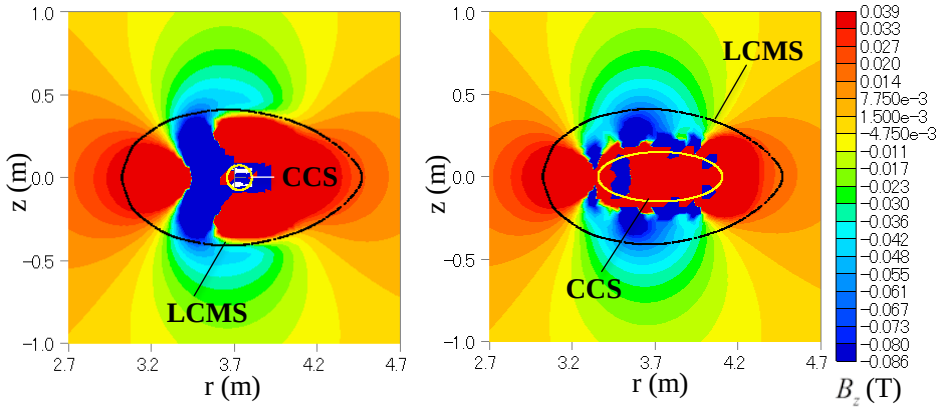

(c) B_z (Left: using the axisymmetric CCS. Right: using the twisted CCS.)

Figure 5. Reconstructed magnetic field caused by plasma current only

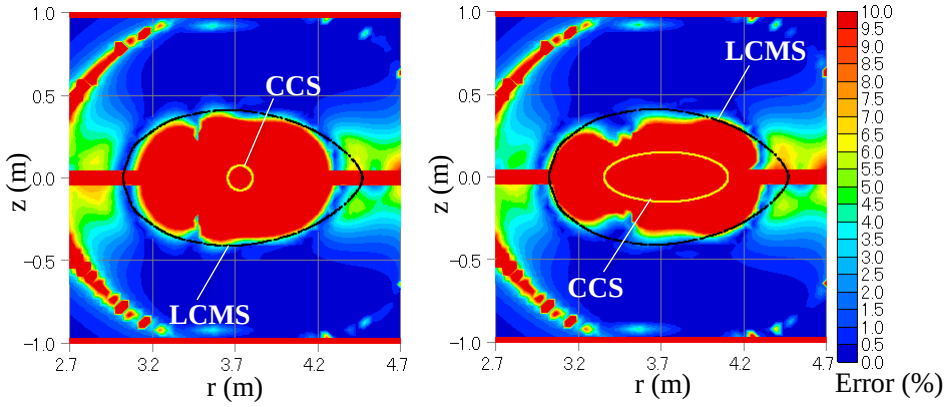

(a) B_r (Left: using the axisymmetric CCS. Right: using the twisted CCS.)

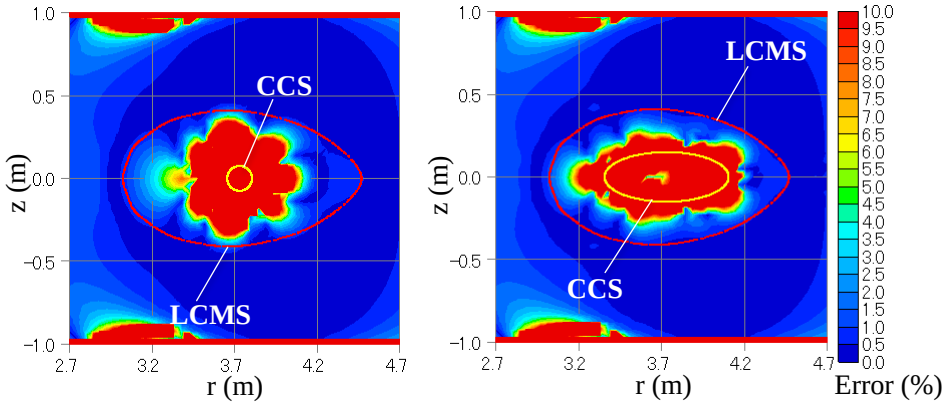

(b) B_φ (Left: using the axisymmetric CCS. Right: using the twisted CCS.)

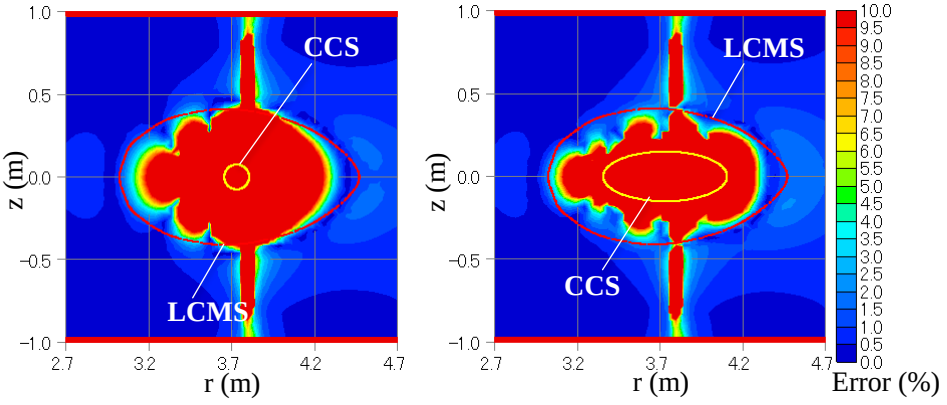

(c) B_z (Left: using the axisymmetric CCS. Right: using the twisted CCS.)

Figure 6. Relative errors of magnetic field caused by both plasma current and coil currents

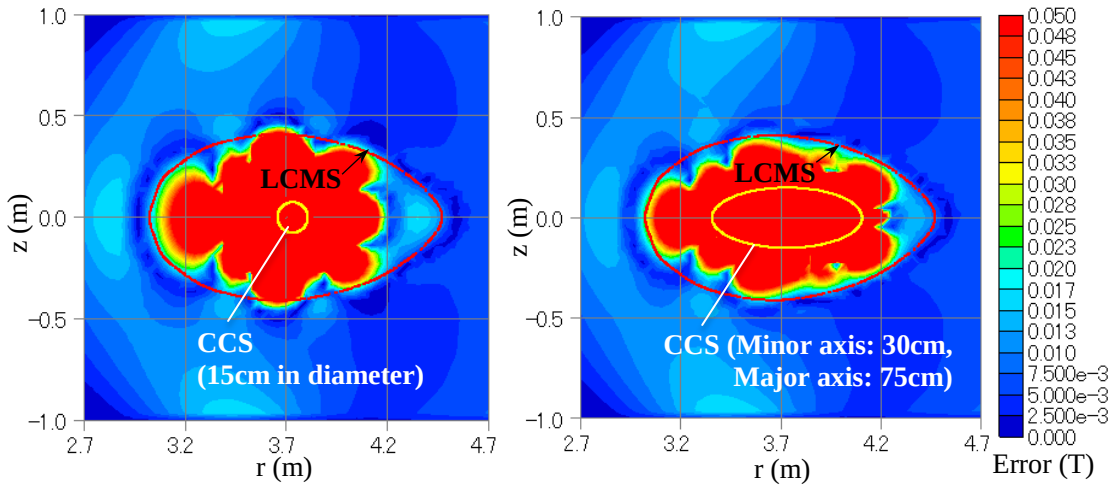

(a) Using the axisymmetric CCS

(b) Using the twisted CCS.

Figure 7. Distribution of absolute error of B_{φ}.

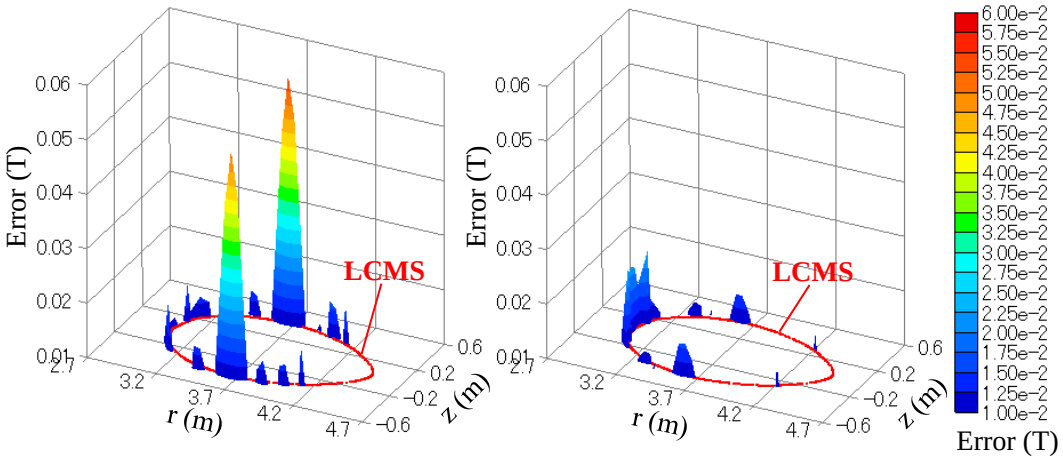

(a) Using the axisymmetric CCS (b) Using the twisted CCS

Figure 8. Absolute errors of B_{φ} near the LCMS

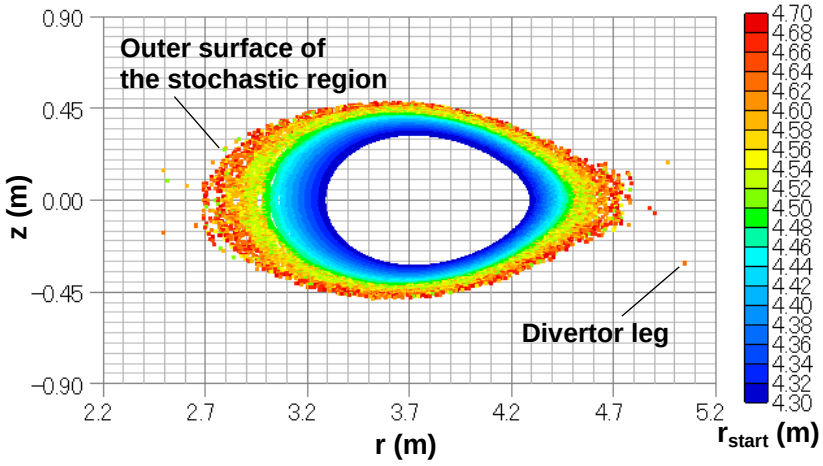

(a) Reference

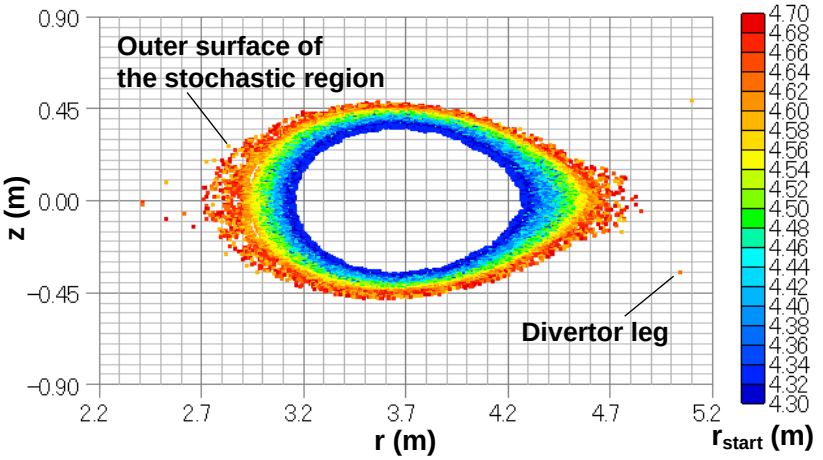

(b) Using the axisymmetric CCS

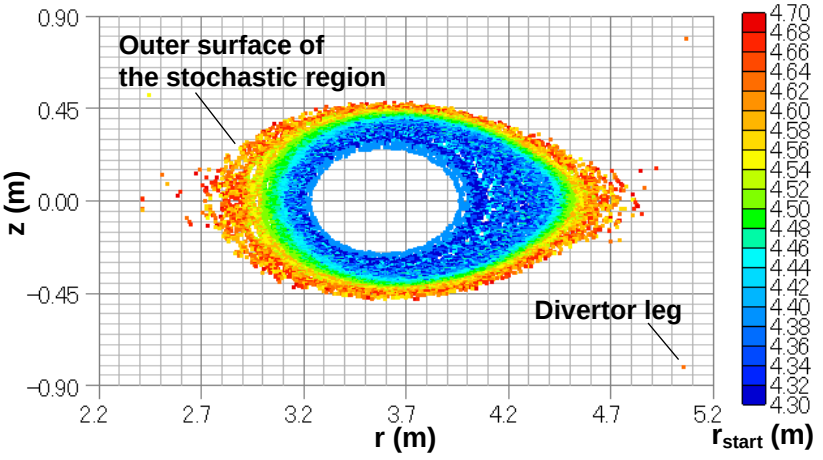

(c) Using the twisted CCS

Figure 9. Poincaré plots of the field line (1): Stochastic region

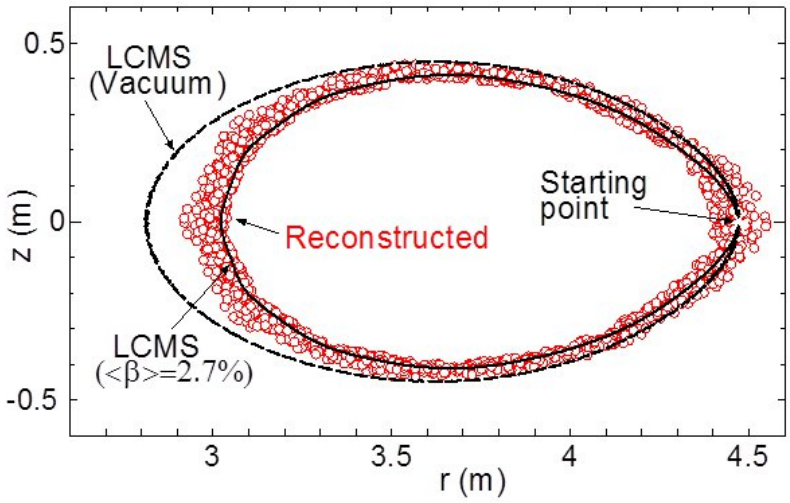

(a) Using the axisymmetric CCS

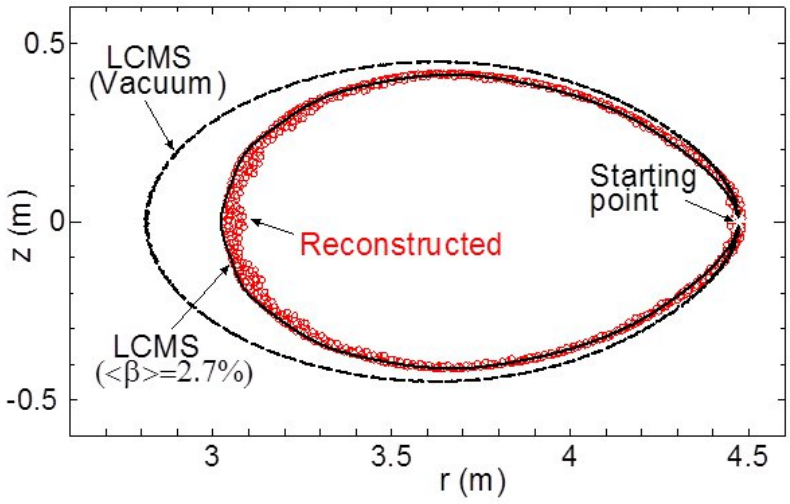

(b) Using the twisted CCS

Figure 10. Poincaré plots of the field line (2): LCMS

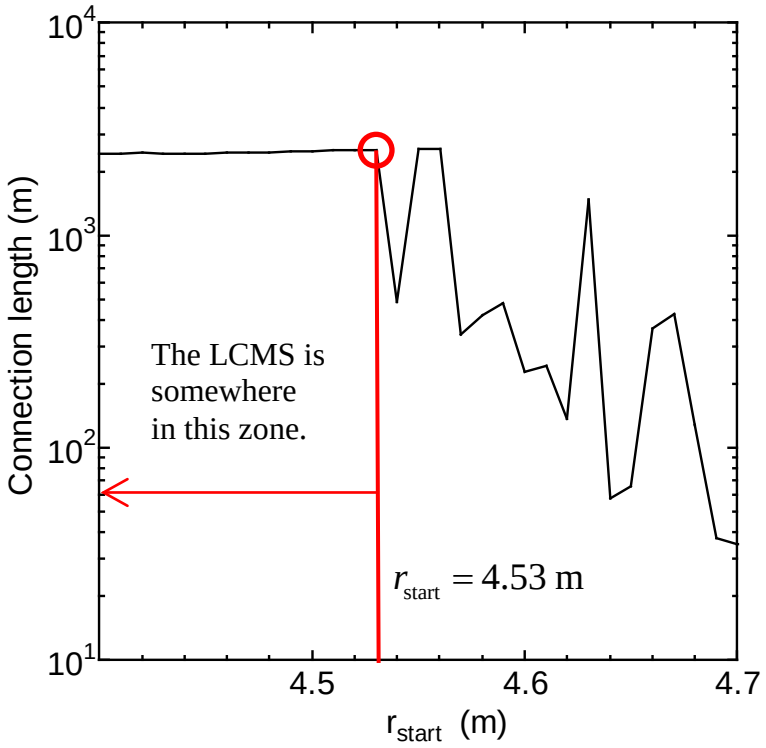

Figure 11. Variation in the connection length

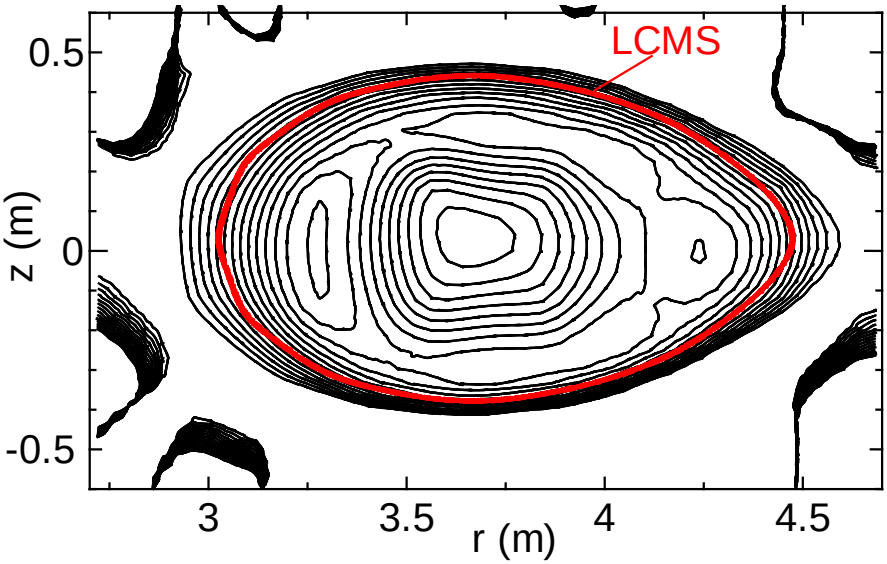

Figure 12. Contours of RBF-built function

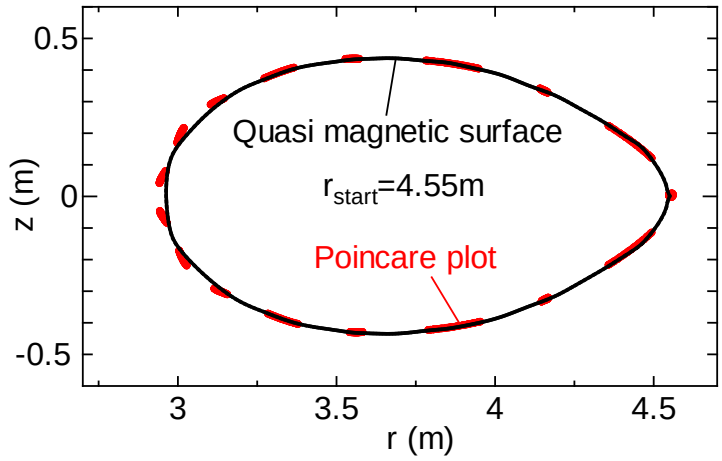

(a) $r_{start} = 4.55\text{m}$

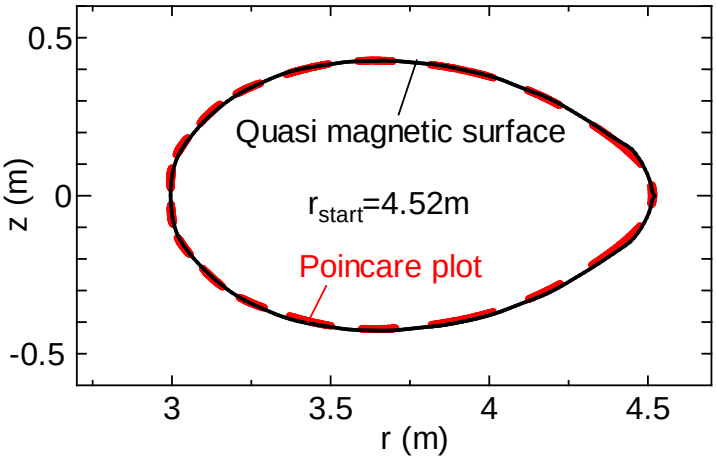

(b) $r_{start} = 4.52\text{m}$

Figure 13. Poincaré plot with the quasi magnetic surface outside the LCMS

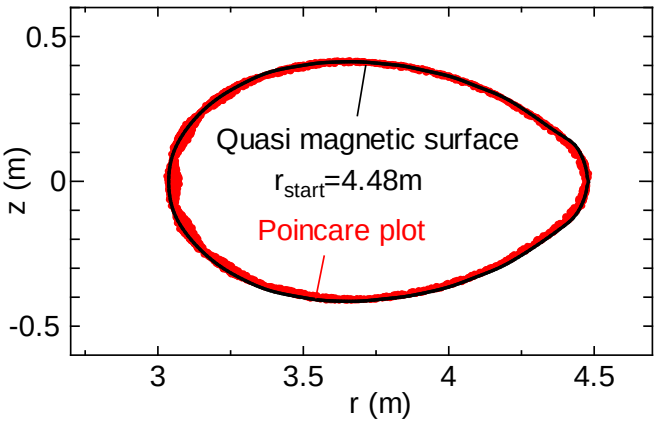

(a) $r_{start} = 4.48\text{m}$

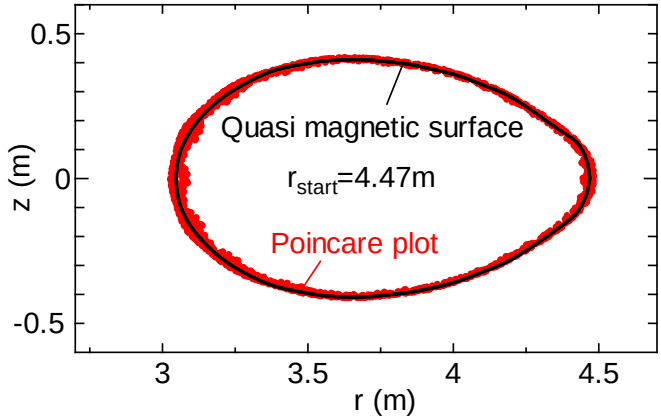

(b) $r_{start} = 4.47\text{m}$

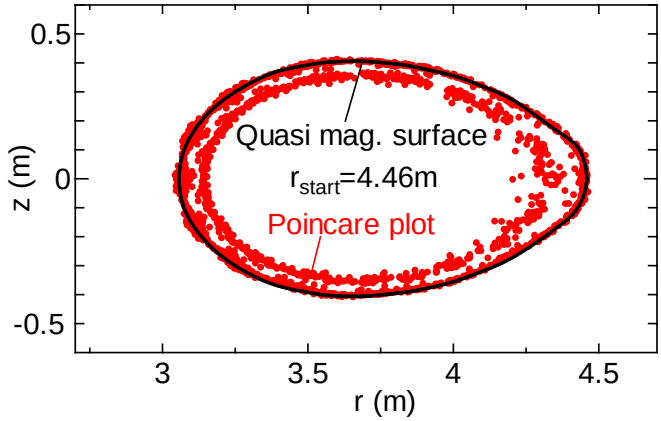

(c) $r_{start} = 4.46\text{m}$

Figure 14. Poincaré plot with the quasi magnetic surface near the LCMS

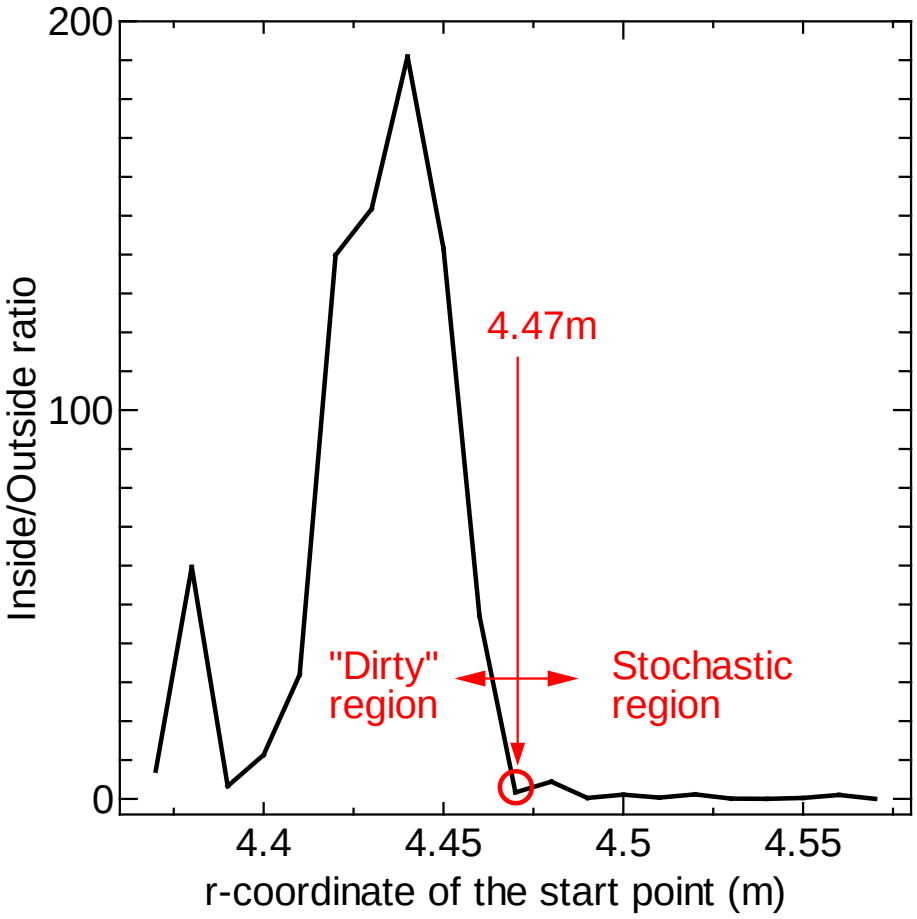

Figure 15. Variation in the ‘inside/outside’ ratio

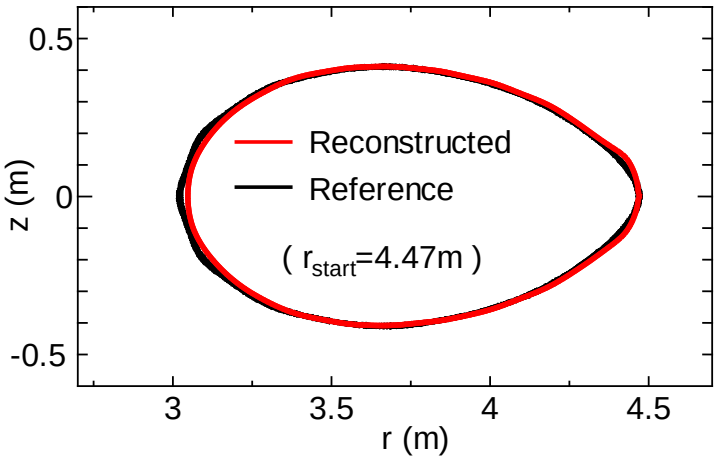

Figure 16. Reconstructed LCMS

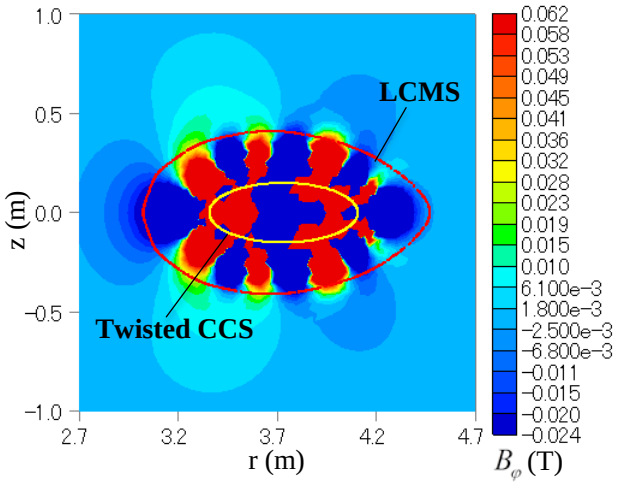

(a) B_φ caused by plasma current

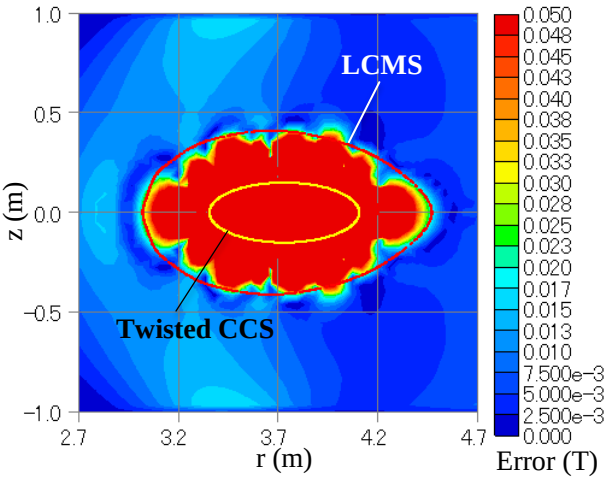

(b) Absolute error

Figure 17. Reconstructed B_φ and its absolute error when the flux loops are not considered

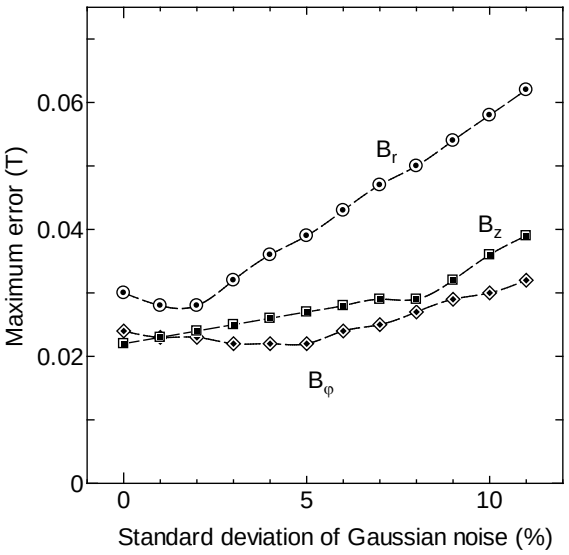

(a) Variation in the maximum errors

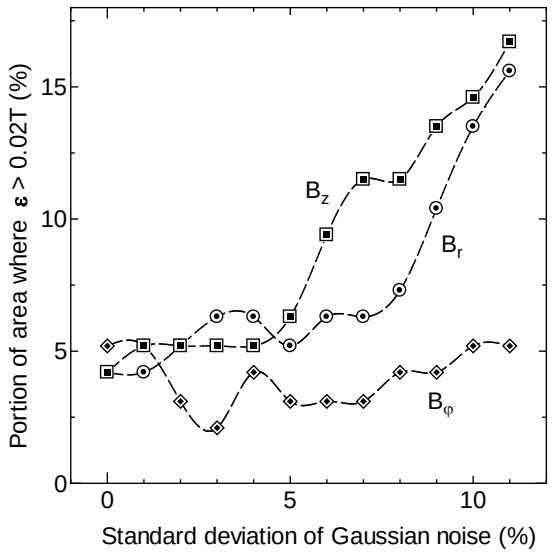

(b) Portion of area where $\varepsilon > 0.02\mathrm{T}$ (%)

Figure 18. Influence of the sensor signal noise

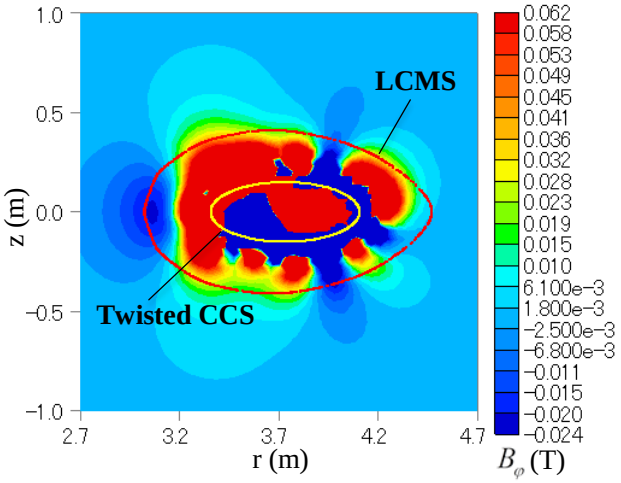

(a) B_φ caused by plasma current

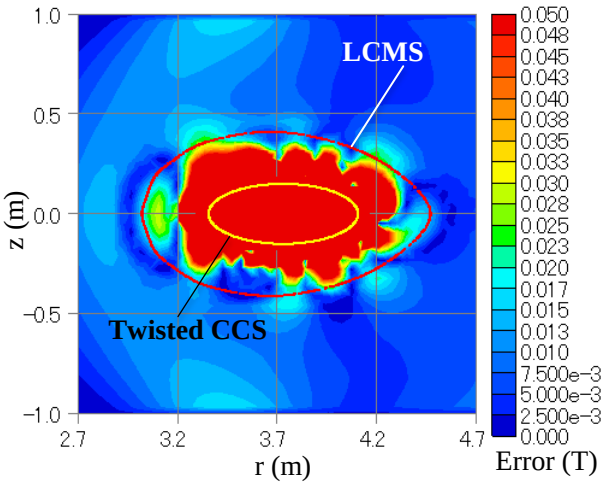

(b) Absolute error

Figure 19. Reconstructed B_φ and its absolute error when the number of sensors and the number of boundary elements are reduced

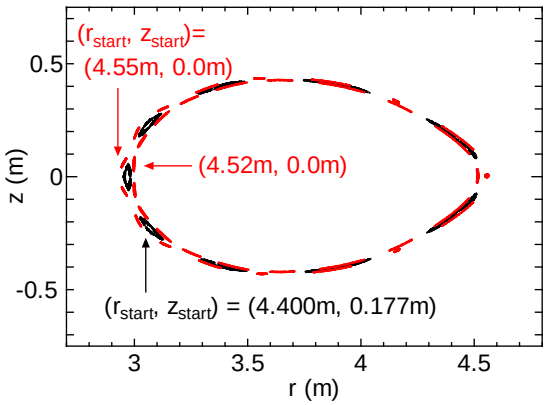

(a) Islands found for the reconstructed field

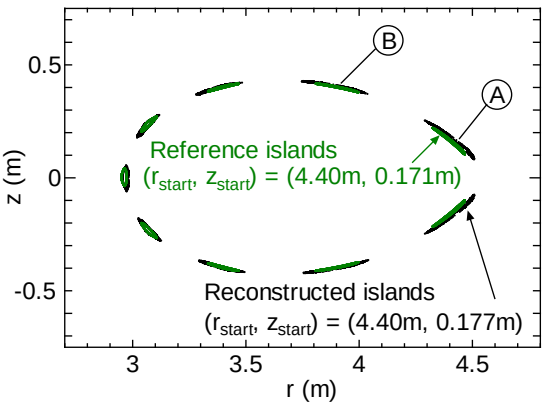

(b) Reconstructed and reference islands

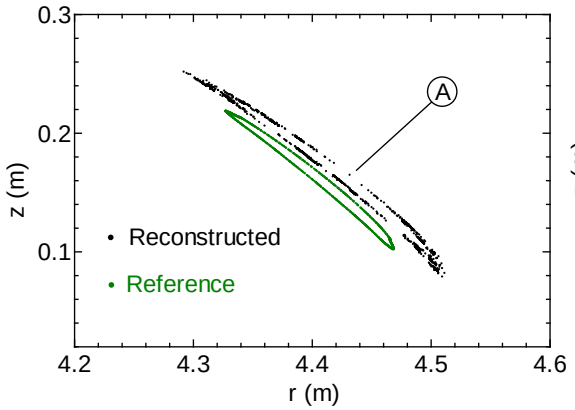

(c) Enlarged island (A)

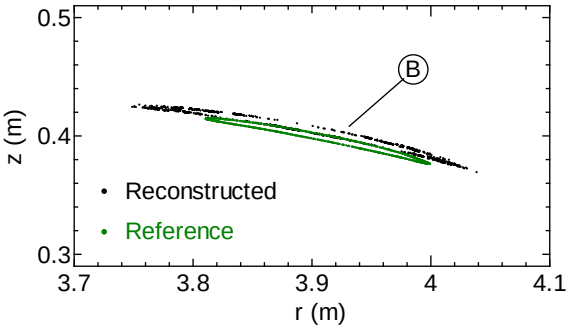

(d) Enlarged island (B)

Figure 20. Magnetic islands

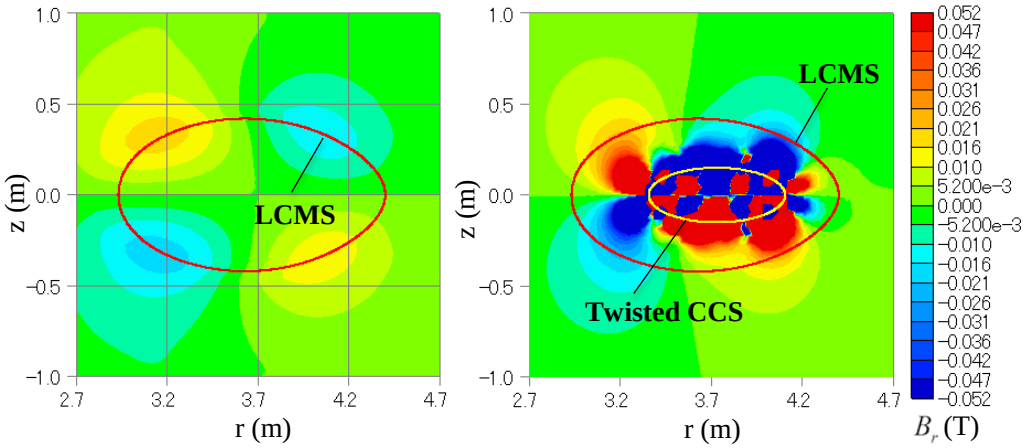

(a) B_r (Left: Reference. Right: Reconstructed.)

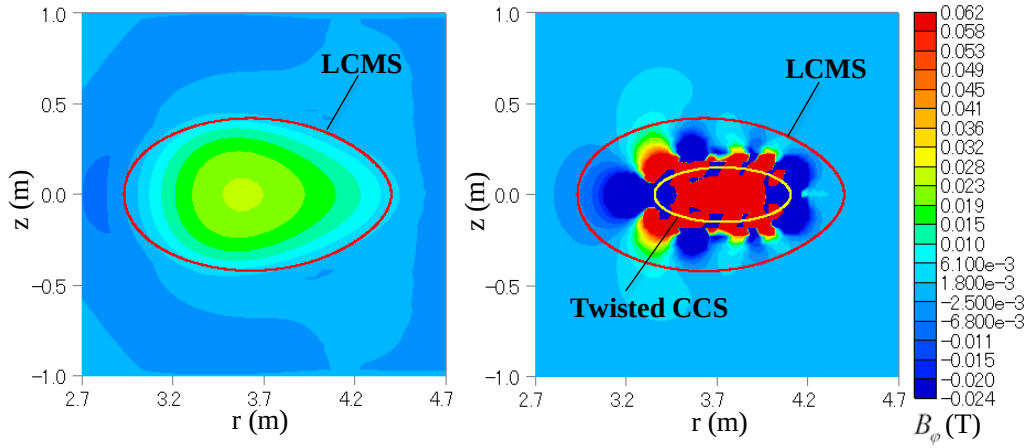

(b) B_φ (Left: Reference. Right: Reconstructed.)

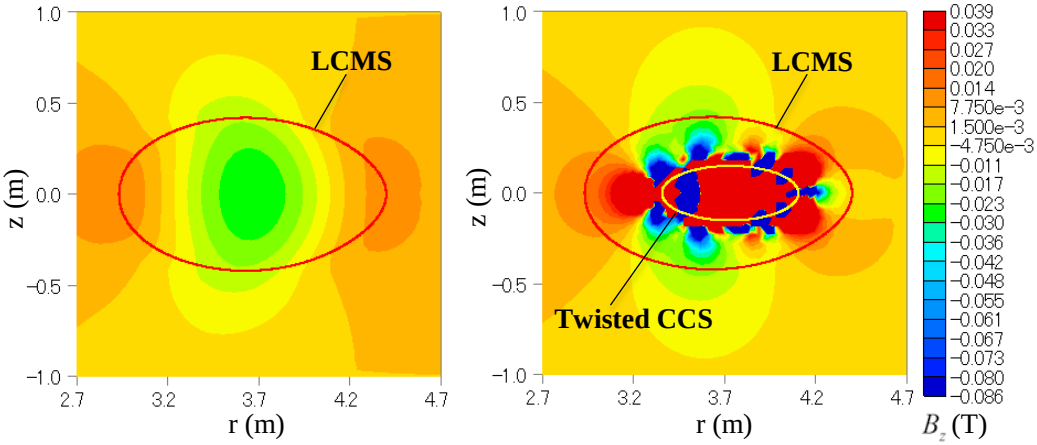

(c) B_r (Left: Reference. Right: Reconstructed.)

Figure 21. Profiles of the reference and the reconstructed magnetic field caused by the plasma current only with $\langle\beta\rangle = 1\%$

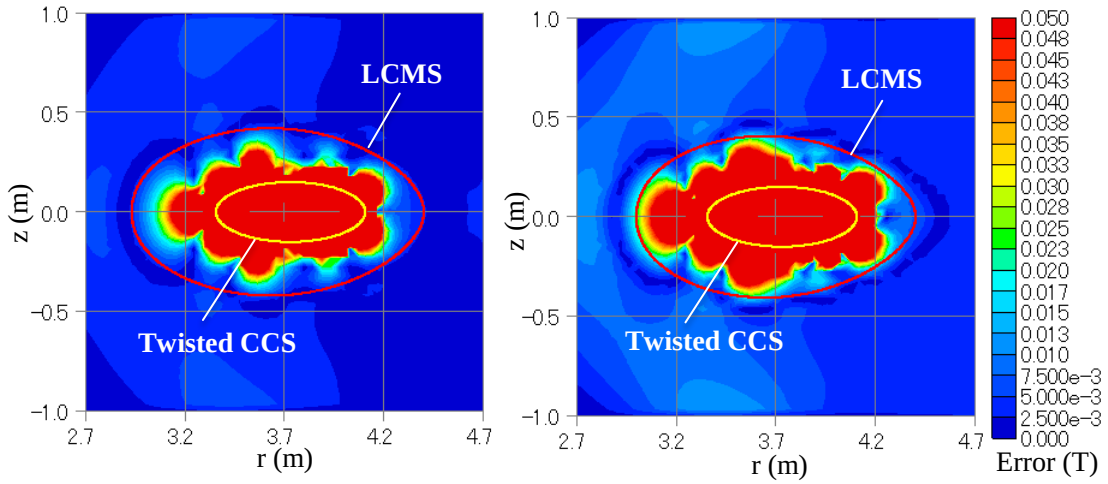

(a) $\langle\beta\rangle = 1.0\%$ (b) $\langle\beta\rangle = 2.0\%$

Figure 22. Absolute errors in the reconstructed B_φ for low β plasmas

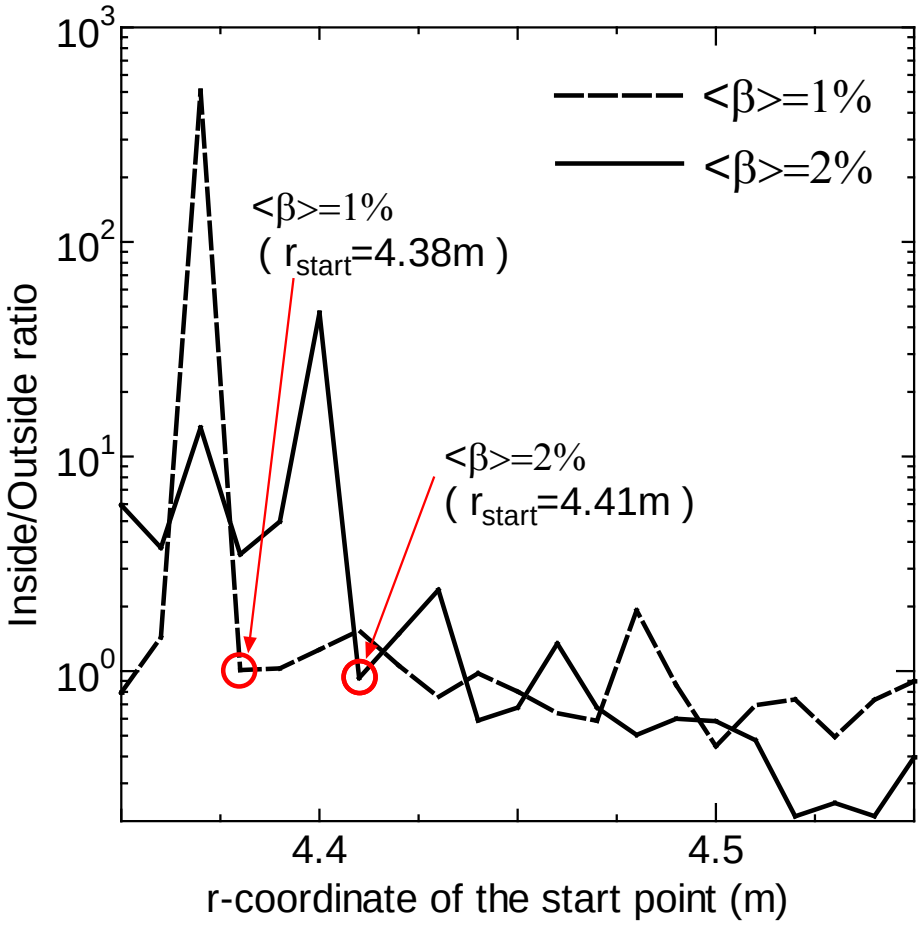

Figure 23. Variation in the 'inside/outside' ratio for low β plasmas

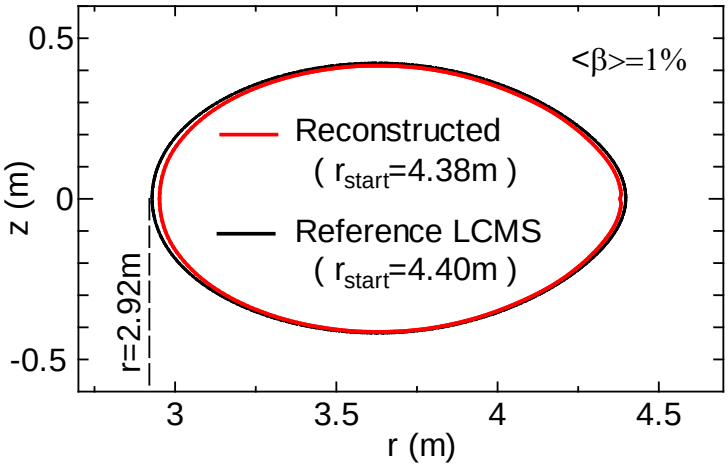

(a) $\langle\beta\rangle = 1.0\%$

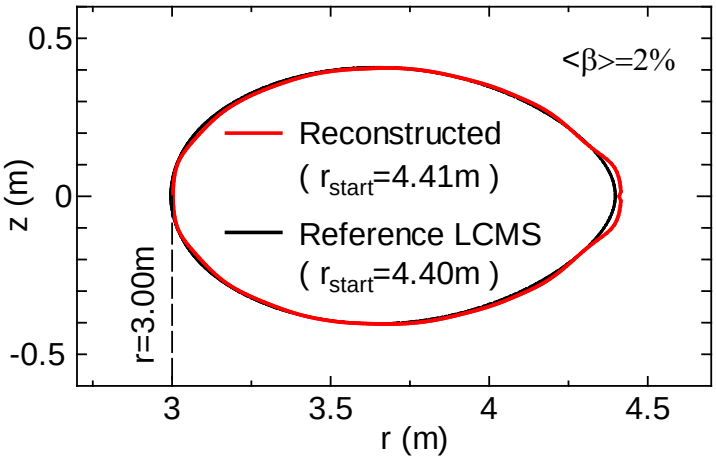

(b) $\langle\beta\rangle = 2.0\%$

Figure 24. Reconstructed LCMS for low β plasmas